AGU PUBLICATIONS

JGR

Journal of Geophysical Research: Space Physics

RESEARCH ARTICLE

10.1002/2013JA018988

Key Points:
- TIDs propagate mainly southward-southeastward for the periods studied
- Horizontal wave phase speeds exceed the ambient lower thermospheric winds
- Vertical wavelengths peak near the altitude where ion velocities are maximum

Correspondence to:
M. J. Nicolls,
michael.nicolls@sri.com

Citation:
Nicolls, M. J., S. L. Vadas, N. Aponte, and M. P. Sulzer (2014), Horizontal parameters of daytime thermospheric gravity waves and *E* region neutral winds over Puerto Rico, *J. Geophys. Res. Space Physics*, *119*, doi:10.1002/2013JA018988.

Received 26 APR 2013
Accepted 19 DEC 2013
Accepted article online 27 DEC 2013

Horizontal parameters of daytime thermospheric gravity waves and *E* region neutral winds over Puerto Rico

Michael J. Nicolls[1], Sharon L. Vadas[2], Nestor Aponte[3], and Michael P. Sulzer[3]

[1]Center for Geospace Studies, SRI International, Menlo Park, California, USA, [2]CoRA Division, Northwest Research Associates, Boulder, Colorado, USA, [3]Center for Geospace Studies, SRI International, Arecibo Observatory, Arecibo, Puerto Rico

Abstract We report on the electron density perturbation amplitudes, periods (up to 60 min), horizontal and vertical wavelengths, phase speeds, and propagation directions of daytime traveling ionospheric disturbances (TIDs) from 115 to 300 km altitude using dual-beam experiments at the Arecibo Observatory (AO), Puerto Rico. As in previous studies, we find a near continuum of waves above the AO. While the TIDs propagate in nearly all directions except purely westward, we find that most propagate southward southeastward. We find that TID amplitudes increase nearly exponentially with increasing period, although with a much smaller slope for periods >30 min. TID amplitudes peak on the bottomside of the *F* region. Typical vertical wavelengths increase from less than 50 km at low altitudes to ~100–300 km. Horizontal wavelengths increase from ~70–100 km to ~150–500 km over the same altitude range. Median vertical wavelengths, horizontal wavelengths, and periods increase with altitude up to $z \sim <225$ km and are approximately constant at higher altitudes. Horizontal phase speeds are >100–150 m/s. We also measure the *E* region horizontal neutral winds and find that they peak at ~150 m/s near $z \sim 105$ km in the middle of the day. Wave phase speeds are in general greater than these ambient winds. In addition, by tracing individual wave packets vertically in altitude, we find that a packet's vertical wavelength generally peaks near the altitude where its inferred ion velocity amplitude is maximum. The vertical wavelength generally decreases above this altitude, an observation that is consistent with gravity wave packet theory.

1. Introduction

Traveling ionospheric disturbances (TIDs) have been observed nearly continuously over the Arecibo Observatory (AO), Puerto Rico using extremely sensitive measurements of plasma density perturbations. These waves can be interpreted as tracers of atmospheric gravity waves (GWs) during the daytime, since the interaction of GWs [*Hines*, 1960] with the ionospheric plasma produces plasma perturbations or TIDs [e.g., *Hooke*, 1968; *Klostermeyer*, 1972; *Kirchengast et al.*, 1996; *Bowman*, 1990]. Mesoscale TIDs (MSTIDs) [e.g., *Kelley*, 2011] have horizontal wavelengths in the range of a few hundred kilometers, periods of tens of minutes to an hour, and corresponding horizontal phase velocities of a few hundred meters per second [e.g., see reviews by *Hunsucker*, 1982; *Hocke and Schlegel*, 1996]. Quantifying the propagation parameters of these waves is important for understanding their sources and their role in driving ionospheric variability.

Various techniques exist to measure the horizontal propagation parameters of the waves, with many recent studies making use of broad arrays of dual-frequency GPS receivers to study the propagation of total electron content perturbations [e.g., *Afraimovich et al.*, 1998, 2000, 2003; *Saito et al.*, 1998, 2001; *Hernández-Pajares et al.*, 2006; *Kotake et al.*, 2006; *Nicolls et al.*, 2004; *Tsugawa et al.*, 2007; *Ishida et al.*, 2008; *Ogawa et al.*, 2009]. All-sky airglow imaging (in particular of the 630 nm OI thermospheric emission) can be used to study the propagation of nighttime MSTIDs [e.g., *Mendillo et al.*, 1997; *Garcia et al.*, 2000; *Shiokawa et al.*, 2003a, 2003b, 2006; *Candido et al.*, 2008; *Seker et al.*, 2009, 2011; *Martinis et al.*, 2010]. HF Doppler sounders are also used to study the horizontal parameters and propagation directions of daytime and nighttime TIDs [e.g., *Crowley et al.*, 1987; *Crowley and Rodrigues*, 2012].

Some TIDs at midlatitudes are observed to propagate southwestward at night [e.g., *Garcia et al.*, 2000; *Shiokawa et al.*, 2003a; *Martinis et al.*, 2010]; these signatures are likely created by midlatitude, nighttime electrodynamic instabilities [e.g., *Behnke*, 1979; *Kelley and Miller*, 1997; *Miller*, 1997; *Kelley and Makela*, 2001; *Otsuka et al.*, 2004]. These TIDs show occurrence rate maxima in the solstices, which may be linked to interhemispheric electric field mapping as well as *E*/*F* region coupling [*Martinis et al.*, 2010]. Such waves should be considered distinct from TIDs created by gravity waves, as discussed by *Crowley and Rodrigues* [2012].

Nighttime, HF Doppler measurements show GWs propagating in nearly every direction, although not necessarily isotropically [*Vadas and Crowley*, 2010; *Crowley and Rodrigues*, 2012]. Other nighttime TIDs observed in 630-nm all-sky imaging have been identified as manifestations of GWs [*Shiokawa et al.*, 2006; *Vadas and Crowley*, 2010]. Detailed studies of the propagation of daytime TIDs at midlatitudes, on the other hand, have shown a tendency for the waves to propagate southward [e.g., *Morton and Essex*, 1978; *Kalikhman*, 1980; *Waldock and Jones*, 1986, 1987; *Crowley et al.*, 1987; *Jacobson et al.*, 1995; *Afraimovich et al.*, 1999; *Hernández-Pajares et al.*, 2006; *Kotake et al.*, 2007; *Ishida et al.*, 2008].

The preferential propagation directions of waves may be the result of a number of physical mechanisms, including critical-level wind filtering of slowly propagating waves [e.g., *Waldock and Jones*, 1984, 1986,1987; *Afraimovich et al.*, 1999], dissipative filtering from molecular viscosity in the thermosphere [e.g., *Vadas and Fritts*, 2005; *Vadas*, 2007] combined with orientation with respect to the background wind [*Fritts and Vadas*, 2008], reflection from increasing temperature and winds [*Fritts and Vadas*, 2008; *Crowley and Rodrigues*, 2012], the influence of local electrodynamics (in particular, ion drag) [e.g., *Liu and Yeh*, 1969; *Kelley and Miller*, 1997; *Kelley*, 2011; *Hernández-Pajares et al.*, 2006; *Kotake et al.*, 2007], discrete azimuth populations [e.g., *Jacobson et al.*, 1995; *Hernández-Pajares et al.*, 2006], and discrete source locations [e.g., *Bristow et al.*, 1994, 1996; *Bristow and Greenwald*, 1996; *Ishida et al.*, 2008; *Ogawa et al.*, 2009; *Vadas and Nicolls*, 2009; *Vadas and Crowley*, 2010]. Occurrence rates of daytime TIDs at midlatitudes tend to peak in winter [*Jacobson et al.*, 1995; *Kotake et al.*, 2007].

While these data sets and studies have been able to characterize TID activity over broad regions, many are limited in sensitivity due to the nature of the measurements and are unable to provide information on the vertical propagation of the waves. Incoherent scatter radar (ISR) measurements, though often unable to provide horizontal propagation information, have been able to assess the vertical propagation of TIDs [e.g., *Oliver et al.*, 1994, 1995, 1997; *Djuth et al.*, 1997, 2004, 2010; *Hocke et al.*, 1996; *Kirchengast et al.*, 1996; *Livneh et al.*, 2007; *Nicolls and Heinselman*, 2007; *Vadas and Nicolls*, 2008, 2009].

Using the phase-steering capability of the Middle and Upper Atmosphere (MU) radar in Japan, *Oliver et al.* [1997] were able to assess the three-dimensional $\mathbf{k}$ vector of medium- and large-scale TIDs in the *F* region, finding typical horizontal phase speeds of 240 m/s, typical vertical wavelengths of 150–200 km, and a slight preference for southward propagation for waves with periods larger than 40 min. More recently, other ISRs have made use of similar phase-steering capabilities to assess the three-dimensional propagation of waves [e.g., *Nicolls and Heinselman*, 2007; *Vadas and Nicolls*, 2008, 2009].

At the Arecibo Observatory, extremely precise and high-resolution measurements of electron density perturbations have revealed nearly continuous imprints of internal atmospheric gravity waves [*Djuth et al.*, 1997, 2004, 2010; *Livneh et al.*, 2007]. *Djuth et al.* [2010] concluded that these waves are locally produced and propagate upward from lower altitudes; they also suggested that internal ocean waves in the Atlantic Ocean to the northeast of the AO are the most likely sources. In this paper, we report on results from the AO where we make use of the beam-steering capability of the radar to extract the horizontal propagation parameters of the observed waves.

2. Experiment and Technique

Experiments were performed at the Arecibo Observatory (18.34°N, 66.75°W) on 23–26 July 2009 to extract the horizontal parameters of thermospheric gravity waves. The Arecibo Observatory is capable of dual-beam measurements, with power split between two antennas, hereafter referred to as the linefeed (LF) and Gregorian (GR) [e.g., *Isham et al.*, 2000]. Observing geometry consisted of pointing the LF vertically and the GR 15° off zenith (75° elevation angle). The observation times and descriptions for the experiments are listed in Table 1. For experiments on 23–25 July, the GR was moved between two azimuths and dwelled for 40–60 min. The two azimuths were 168° (SSE), which lies along the local magnetic meridian, and 78° (EEN), which is a 90° counterclockwise rotation. The fastest slew rate possible was used to move between the two positions, with the GR taking about 4 min to move 90°. The geometry for this configuration is shown in Figure 1 at an altitude of 200 km (left). Figure 1 (right) shows the distance between the GR and LF beams as a function of altitude. This distance varies from ∼30 km at 100 km altitude to ∼100 km at 400 km altitude. On 26 July, a slightly different setup was employed, which consisted of continuous antenna motion between azimuths 123° and 213° (168° ± 45°).

Table 1. Observation Days

Date	Observation Time (UT = AST+4 h)	Dwell Time (min)
23July2009	1030–1900 AST	40
24July2009	0715–1900 AST	60
25July2009	0715–1900 AST	40
26July2009	1015–1900 AST	N/A (see text)

The technique used for the derivation of the horizontal wave parameters is similar to that described in Nicolls and *Heinselman* [2007] and *Vadas and Nicolls* [2009] (applied to the Poker Flat Incoherent Scatter Radar), with the additional assumption of wavefield stationarity over an entire dwell period. Wave periods and vertical wavelengths can be derived directly from vertical measurements of ionospheric density and/or velocity fluctuations. Measurements of the same waves from additional look directions provide information on the horizontal propagation of the waves, assuming the wave is propagating but not changing (in amplitude due to dissipation, for example) over the observation volume. In general, two additional beams would be necessary to derive the full wave $\mathbf{k}$ vector; at Arecibo, we must rely on antenna motion to give this additional information. The GR measurements provide information on the horizontal wavelength of the observed wave: a wave propagating over the field of view will have a phase shift associated with its propagation time (wave phase speed). If the wave is stable for several periods and is observed both in the southward and eastward looking measurements, then a full horizontal wavenumber vector can be derived, giving the propagation direction and wave phase speed.

With this technique, sensitivity and spatial aliasing can be an issue. Waves with very long horizontal wavelengths (for example, the inertia-gravity wave observed by *Nicolls et al.* [2010]) are essentially stationary over the field of view; waves with very short horizontal wavelengths (less than the separation distance of the beams) would be spatially aliased. For the Arecibo measurements, the dwell/motion time of the system provides additional uncertainty: (1) For a standard Fourier analysis, it is not possible to resolve wave motions with periods longer than the dwell time and (2) given the time stationary requirement of the Arecibo measurements, for unambiguous $\mathbf{k}$ vector determination, the wave packet must be stationary over two full dwells (one observation at each look direction). Both of these issues are serious but neither precludes analysis: For example, a correlation analysis can yield average time delay for density perturbations, and one component of the $\mathbf{k}$ vector for a given wave packet may be enough if other assumptions about the wave's parameters can be made.

The GW measurements critical to this study are observed indirectly through electron density perturbations, which are caused by periodic advection and compression of plasma as the neutral winds of the GWs push

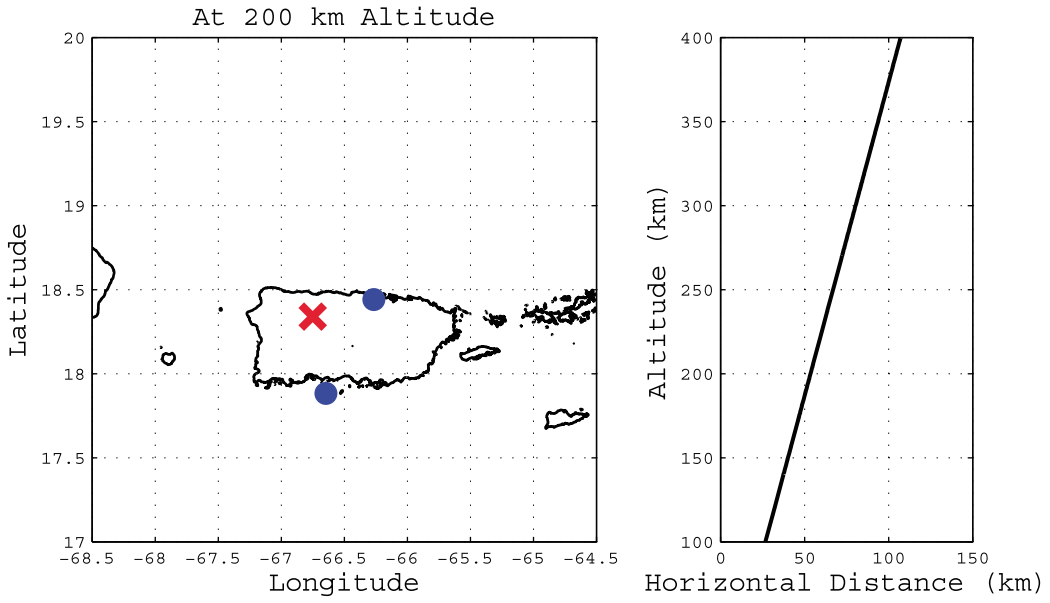

Figure 1. (left) Geometry for Arecibo experiments. Red cross indicates the location of Arecibo as well as the pointing direction of the linefeed antenna. The blue circles denote the two Gregorian antenna pointing positions used for the experiments from 23 to 25 July. (right) Horizontal distance between the beams as a function of altitude for the off-zenith angle of 15°.

and pull the plasma along the field lines [e.g., *Hocke and Schlegel*, 1996; *Vadas and Nicolls*, 2009]. The electron density measurements are made using one of the most precise ground-based ionospheric diagnostics in existence: probing of the plasma line. The plasma line resonance occurs close to the plasma frequency as predicted by incoherent scatter theory [e.g., *Dougherty and Farley*, 1960; *Salpeter*, 1960, 1961]. The information in the plasma line resonance lies in the frequency of the return, not in the shape of the spectrum, as is the case for the ion line. Frequency measurements are much more accurate than power/amplitude measurements (since they do not depend on receiver gains and system losses, which are often difficult to measure and variable) so using the plasma line resonance frequency as an ionospheric diagnostic is particularly useful [e.g., *Nicolls et al.*, 2006; *Aponte et al.*, 2007]. A modern coded long pulse (CLP) [*Sulzer*, 1986a] technique has been developed to probe the plasma line [*Djuth et al.*, 1994]. This technique allows the plasma line resonance frequency to be measured very accurately as a function of altitude with high range resolution (up to 75 m) and high time resolution (a few seconds). The statistical accuracy of the measurements is close to 0.02%. The experimental scheme utilized in this study consisted of transmitting 40 s of a randomly coded 1 μs baud pulse, 10 s of a multifrequency long-pulse mode [*Sulzer*, 1986b] and 10 s of a Barker-coded pulse for power profile measurements in sequence. The CLP was used to compute ion line spectra as well as plasma line spectra, with the latter sampled through 5 MHz digital filters centered around the upshifted plasma line from 3 to 8 MHz on both the LF and GR.

A peak-finding algorithm was used to identify plasma line signatures and determine the electron density, subsequently averaged over 1 min and ∼2 km in range. In order to identify gravity wave signatures, continuous measurements from the vertical-looking beam (LF) were filtered for wave motions with less than 2 h periods. Because of the discontinuous nature of the off-vertical beam (GR) measurements, electron density measurements were instead detrended over each dwell period with a simple polynomial fit.

3. Observations

3.1. Electron Density Perturbations

Figure 2 summarizes the calibrated electron density measurements and perturbations from the first 3 days of observations, which will be the focus of this paper. Periods where plasma line signatures could not be determined are indicated by the white areas. Figure 2 (first row) shows the N_e measurements for the 3 days, with significant and clear daily variation in the background electron density, likely driven by a number of electrodynamic phenomena. The first day (23 July 2009) shows two peaks in N_e at about 14 and 18 AST (UT = AST+4 h). The 24 and 25 July show peak electron densities of close to 10^{12} m^{-3} between 16 and 18 AST.

The fractional electron density perturbations ($\delta N_e/N_e^0$) from the continuous time series (LF, vertical beam; Figure 2, second and third rows) show clear wave motions on all 3 days. Short period, short vertical wavelength waves are seen at lower altitudes. The largest-amplitude perturbations are seen on the bottomside of the *F* region (∼200–250 km), as expected [e.g., *Vadas and Nicolls*, 2009], with relatively long periods (40–60 min) and large vertical wavelengths (i.e., lines of constant phase that are close to vertical). Peak perturbation amplitudes are in the 5–10% range. Wave perturbations are also seen in the off-vertical beam (GR, lower panels). Because the wave phases move downward in time, these measurements indicate upward propagating GWs.

3.2. Wave Spectra

The spectral properties of the waves are summarized in Figure 3. One hour running Lomb-Scargle spectrograms were performed on the LF data sets. Frequency bins with false alarm probabilities of greater than 50% were eliminated, and the spectrograms were averaged over the altitudes indicated in each panel and in the figure caption. Spectrograms from 115 to 250 km are plotted.

The upper altitudes, especially on 23 and 24 July, are dominated by wave packets with periods of 40–60 min lasting for ∼>1 h. On 25 July, some shorter period (τ_r ∼25–30 min) waves are seen prominently. At lower altitudes, these large-period waves are also observed, but in addition there is significantly more shorter-period and temporally localized wave activity. Of note are localized wave packets seen in multiple altitude bins. For example, on 24 July a wave packet with a period of 30–60 min is observed at ∼14 AST, lasts for ∼30 min and is seen in the 120–130 km bin all the way up to the 225–275 km bin. In addition, this wave packet appears to be seen first at the higher altitudes, implying a correlation due to source effects; i.e., the apparent temporal correlation seen in the multiple range bins may be due to a common source driving the waves, and the apparent time shift due to higher phase speed waves penetrating to higher altitudes and arriving prior

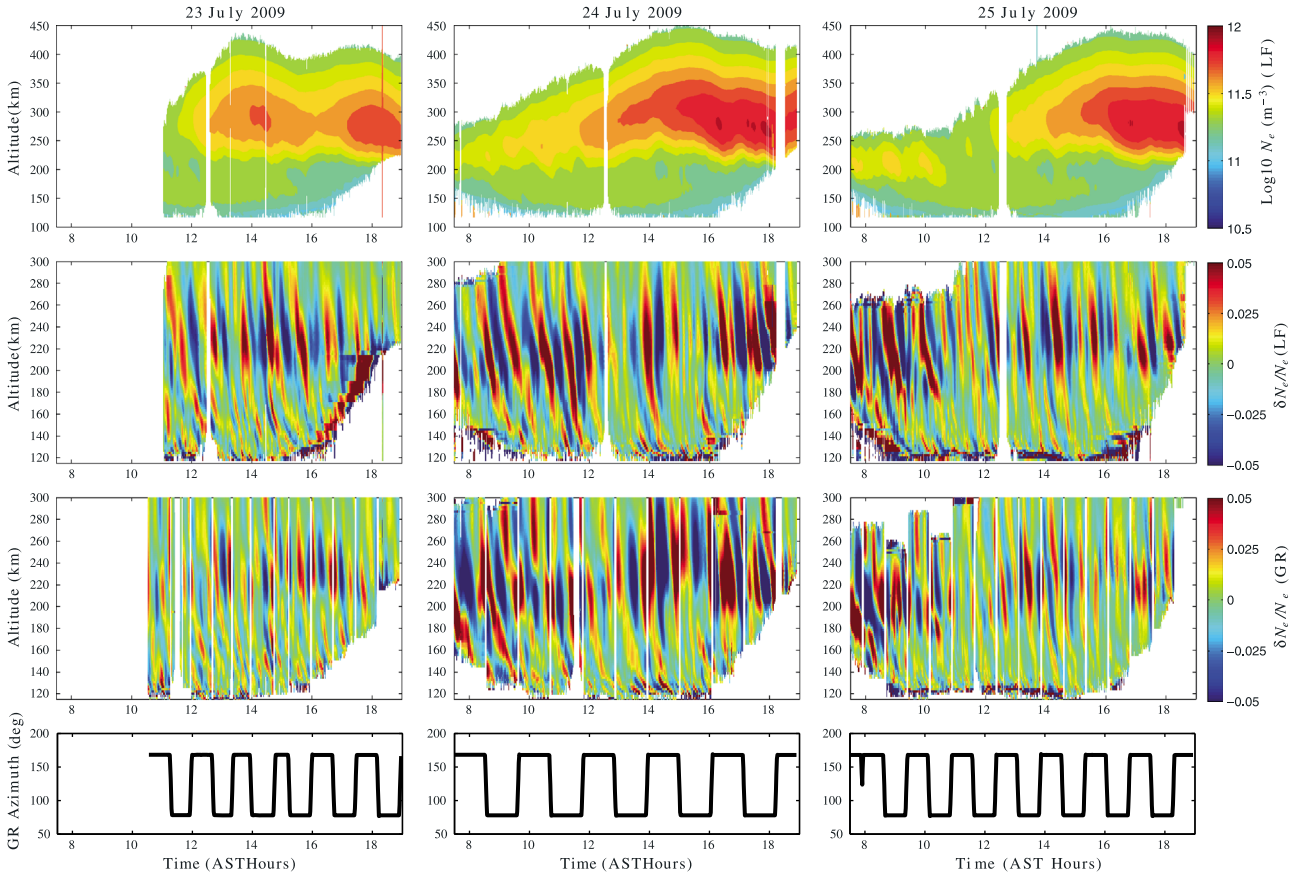

Figure 2. (first row) Log_{10} of N_e (second row) $\delta N_e/N_e$ for vertical looking beam (LF). (third row) $\delta N_e/N_e$ for off-vertical looking beam (GR). (fourth Row) Off-vertical beam (GR) azimuth angle.

to the lower phase speed waves. This trend is not unusual in the spectrograms shown in Figure 3, with a general trend being longer and more continuous wave activity at higher altitudes.

3.3. Wave Parameter Determination

An example of a particular time period in more detail is shown in Figure 4, from 10 to 18 UT on 25 July analyzing the altitude range 165–185 km. Figures 4a and 4b show the fractional N_e perturbations for the two beams (LF and GR), with the white stripes in Figure 4b representing the repositioning period between dwells. There is high correlation for the perturbations observed by the two beams, as seen in the line plots in Figure 4c. In this panel, the continuous black line represents the $\delta N_e/N_e^0$ observed in the vertical beam, and the colored lines represent the $\delta N_e/N_e^0$ observed in the off-vertical beam for the EEN viewing direction (blue) and the SSE viewing direction (red). However, there is also clear phase variation between the two curves: For example, note the dwell to the EEN (blue) from ~ 13.14 to 13.79 AST as compared to the subsequent dwell to the SSE from ~ 13.89 to 14.54 AST. In the EEN direction, the perturbations as observed by the two beams are nearly in phase. In the SSE direction, there is a clear phase variation, with the LF perturbations leading the GR perturbations. These observations imply phase fronts aligned in the EEN direction and propagating mainly to the SSE. This motion is quantified by performing a cross correlation over each dwell and each altitude. The phase at peak correlation is determined, and the median and standard deviation of this phase over all altitudes is assessed. The median peak correlation was over 0.85 for this time period (~13.14–14.54 AST).

Figure 4d shows the mean spectrogram for this time and altitude range, where the period at maximum amplitude is traced out (black solid line). Figure 4e shows the averaged period at maximum amplitude over each dwell (red, right axis), which is in the range 30–40 min for the time period discussed. An apparent wave phase velocity along the EEN and SSE directions is determined as $\delta x/\delta t$ where δx is the separation distance of the two beams (which varies with altitude; see Figure 1), and δt is the phase delay in seconds. This apparent phase speed is plotted as the black lines with error bars representing the standard deviation of the

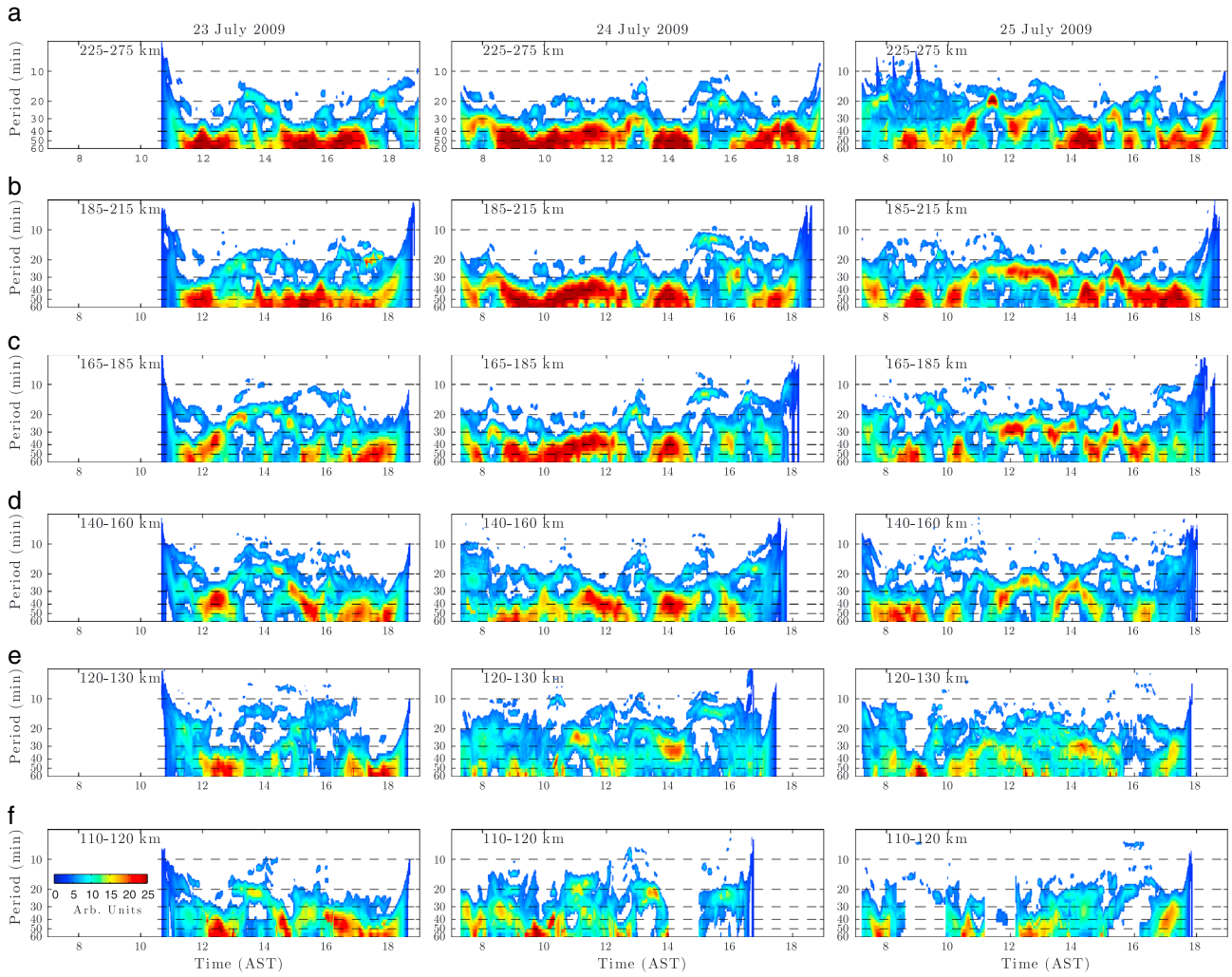

Figure 3. Average spectrograms for 23–25 July for six different altitude bins: (a) 250 ± 25 km, (b) 200 ± 15 km, (c) 175 ± 10 km, (d) 150 ± 10 km, (e) 125 ± 5 km, (f) 115 ± 5 km.

measurements. Note that this apparent phase speed measurement is not the true phase speed of the wave (neither is it a projection, since the phase speed of a wave is a scalar quantity defined by ω_r/k_H where ω_r is the ground-based radian frequency of the wave and $k_H = 2ß/\lambda_H$ is the horizontal wavenumber of the wave) but is simply an apparent speed determined by the time delay over the distance δx. The apparent velocity is 548 ± 20 m/s when viewing in the EEN direction and 132 ± 17 m/s when viewing in the SSE direction. Given these measurements, and a mean period of 35 min, we infer a horizontal wavelength of 275 km and a propagation azimuth (east of north) of 155°, or to the SSE, as postulated. The true horizontal phase speed of this wave would be ~130 m/s.

More generally, wave propagation parameters are determined in the following manner. For a given dwell period, and for all altitudes, a cross-spectral analysis is done between the time series of electron density perturbations observed in the vertical direction (LF) and in the off-vertical direction (GR). A peak-finding algorithm is employed to pick out statistically significant spectral peaks. In this way, waves with significance over a predetermined level of noise, as well as the phase delay for each wave individually, can be extracted. Additional constraints are enforced where a wave at some period must exist at multiple adjacent altitudes and must have a minimum amplitude.

This analysis yields a phase delay ζ_{ij} and cross-spectral TID amplitude for each wave. The phase delay between two measurements is related to the wavenumber by approximately,

$$k_{m,ij} = \mathbf{k} \cdot \hat{\mathbf{k}}_{r,ij} \approx \frac{\delta\zeta_{ij}}{\delta x_{ij}} \quad (1)$$

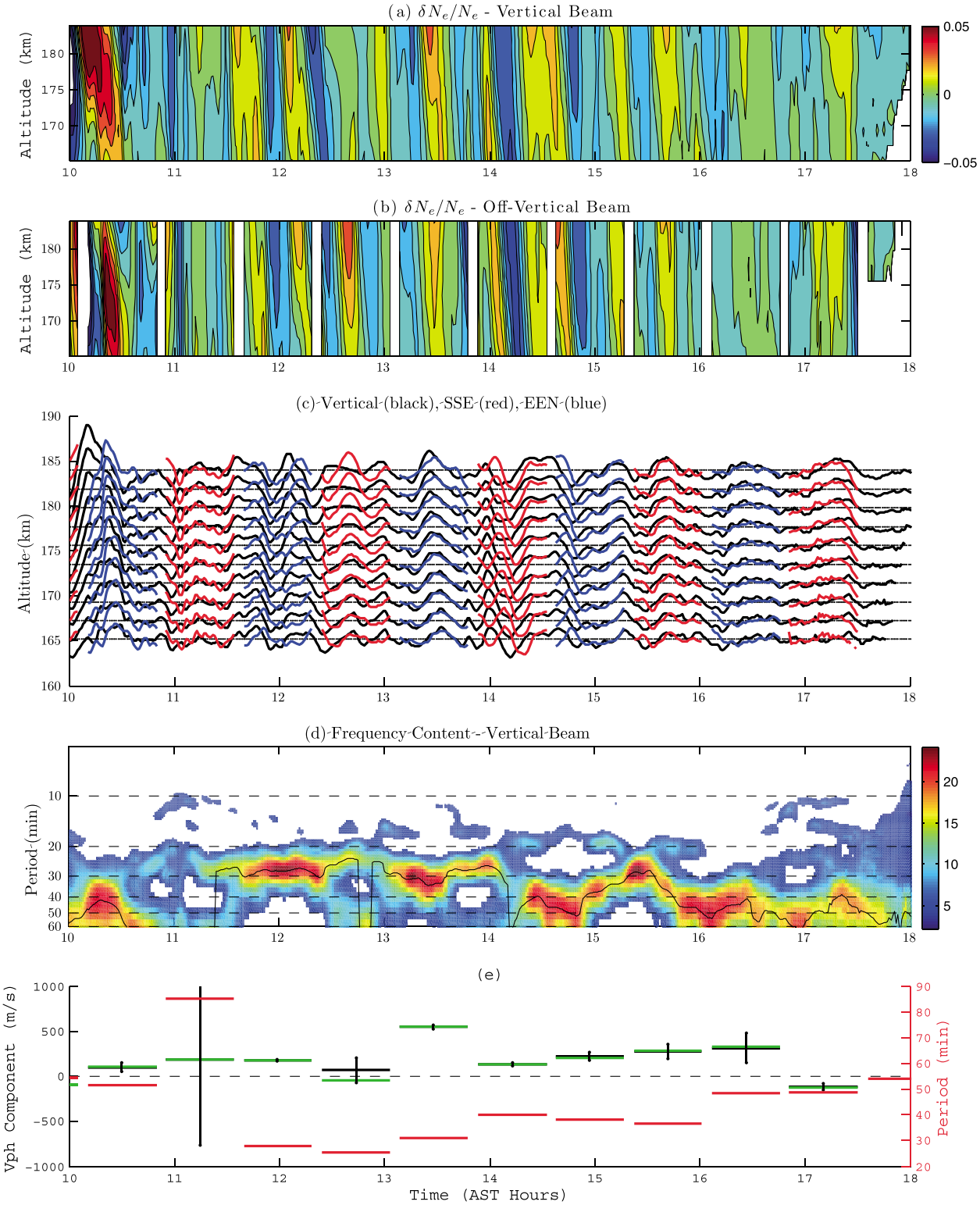

Figure 4. For the period 10–18 UT on 25 July: (a) $\delta N_e/N_e$ from the vertical beam, (b) $\delta N_e/N_e$ from the off-vertical beam, (c) line plots of $\delta N_e/N_e$ from the two beams overlaid (black = LF, colored = GR), (d) spectrogram, with black line indicating period at maximum TID amplitude, (e) mean period (red) for each dwell (right axis) and two estimates of the component phase velocity (black and green) with vertical error bar representing the spread of the data (left axis).

where $\mathbf{k} = (k, \ell, m)$ is the wavenumber vector of a wave with radian frequency ω_r, $\hat{\mathbf{k}}_{r,ij}$ is the unit vector between measurements i and j, $\delta\zeta_{ij}$ is a measured phase delay in radians, and δx_{ij} is the separation distance between the measurements i and j. For phase delays at a given altitude with one beam ($i = 1$) pointed vertically, $\hat{\mathbf{k}}_{r,1-2}$ is horizontal and equal to $(\sin\theta, \cos\theta, 0)$ where θ is the azimuth angle of the off-vertical beam (the Gregorian antenna in this case, $j = 2$). The approximation in equation (1) comes from the fact that there may be additional phase delays induced by the measurement technique. The measured phase delay may include contributions from effects other than GWs, such as varying electron densities, as discussed later and in Appendix B.

Measurements from different pointing positions can then be used to determine the horizontal wavenumber vector. Practically, to determine a given wavenumber vector, we use measurements from the subsequent dwell where a wave at a similar frequency, similar amplitude, and similar altitude has been observed (note that we do not actually cross-correlate the measurements at different times from the two different look directions, but assume that if a wave with a similar amplitude and period is present at the same altitude, that we can use it to resolve the propagation direction). The horizontal wavenumber vector, $\mathbf{k}_H = (k, \ell)$, is then determined by solving the linear least squares problem,

$$\mathbf{k}_H = \mathbf{A}\mathbf{k}_m \tag{2}$$

where $\mathbf{A}$ is a geometry matrix (typically size 2×2 if only two measurements are used) with rows corresponding to the first two elements of $\hat{\mathbf{k}}_{r,1-2}$ or $\hat{\mathbf{k}}_{r,1-3}$ above (denoting beam #1 as the vertical measurements, and beams #2 and 3 as the off-vertical measurements) and $\mathbf{k}_m$ is a column vector of measurements $k_{m,ij}$.

Vertical wavenumbers are determined in a similar fashion. In this case, perturbations are analyzed between adjacent altitudes using the vertically pointed beam, and we obtain simply

$$\mathbf{k} \cdot \hat{\mathbf{k}}_{r,1-1} = m \approx \frac{\delta\zeta_{ij}}{\delta z}. \tag{3}$$

Again, note that equation (3) is only an approximation to GW phase because of the contribution of additional phase delays. For the case of vertical wavelength measurements in particular, the effects of a changing electron density scale height may be important. In Appendix B, we derive a correction to the phase delay measurements for the case of vertical wavelength measurements that includes the changing electron density scale height of the medium. We employ this correction only when analyzing the vertical wavelengths later in this paper; in general, we ignore these additional phase terms, for both horizontal and vertical phase delay measurements, and thus, our results should be considered measurements of TID parameters rather than direct observations of GW parameters.

4. Results and Discussion

4.1. Wave Propagation Directions

Wave parameters were determined using the techniques described in section 3.3 for all altitudes and local times. Histograms of wave propagation directions for the 3 days are shown in Figure 5. The histograms have similarities and differences across the 3 days. On 23 and 25 July, a predominance of southward and southeastward propagating waves is observed, especially on 25 July, and a smaller number toward the northeast. Very few waves are observed to propagate to the west. On 24 July, a more isotropic distribution is observed, but again, a predominance of southward going waves is apparent. A significant number of northward propagating waves are also apparent on this day. Overall, the histograms show a significant minimum of westward propagating waves and a preference for southeastward going waves.

The observation of a peak in southward/southeastward going waves during the day is consistent with previous low-latitude and midlatitude measurements. *Waldock and Jones* [1986], making observations using the HF Doppler technique at a higher latitude (52°N), show a maximum in propagation direction toward the southeast. *Jacobson et al.* [1995], using very long baseline interferometry illuminated by VHF radio beacons in New Mexico (36°N), also observed a preponderance of southward going waves during the day and transitioning to westward/northwestward going waves in the late evening through local midnight. However, the results of *Jacobson et al.* [1995] show essentially a bimodal azimuth distribution (southward during the day, westward-northwestward at night), which, they argue, suggests that wind filtering cannot explain the preferred azimuths. The results of *Oliver et al.* [1997] at the MU radar in Japan (34°N) show a slight preference for southward going waves.

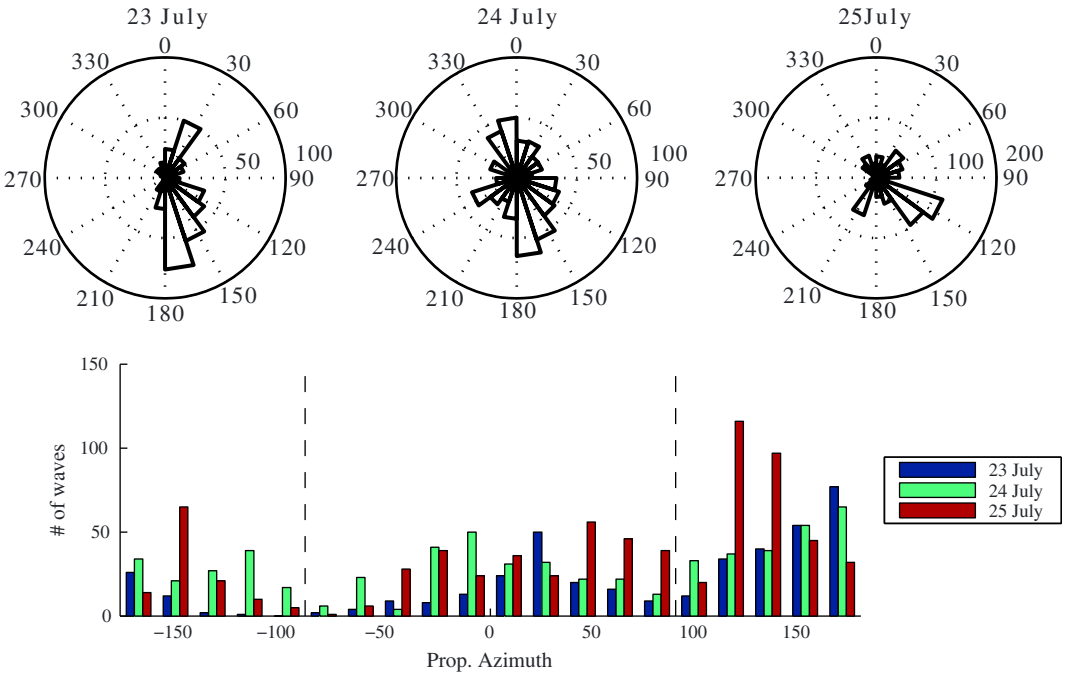

Figure 5. Propagation direction histograms for 23, 24, and 25 July.

Determining how preferred wave propagation directions change with time sheds light on the sources of the waves and the role of effects like wind filtering and dissipation in determining the population of waves reaching the thermosphere [e.g., *Waldock and Jones*, 1984, 1987; *Vadas*, 2007]. In Figure 6, we plot the fraction of waves going northward ($-90° < \phi < 90°$), southward ($-180° < \phi < -90°$, $90° < \phi < 180°$), eastward ($0° < \phi < 180°$), and westward ($-180° < \phi < 0°$) as a function of time in 2 h bins for all 3 days of observation. For this plot, each wave is assigned to be going either northward or southward and either westward or eastward (so the sum of the fractions is 2). On all 3 days, waves propagate increasingly northward as the day progresses. On 23 and 25 July, we see a very strong preference for eastward going over westward going waves.

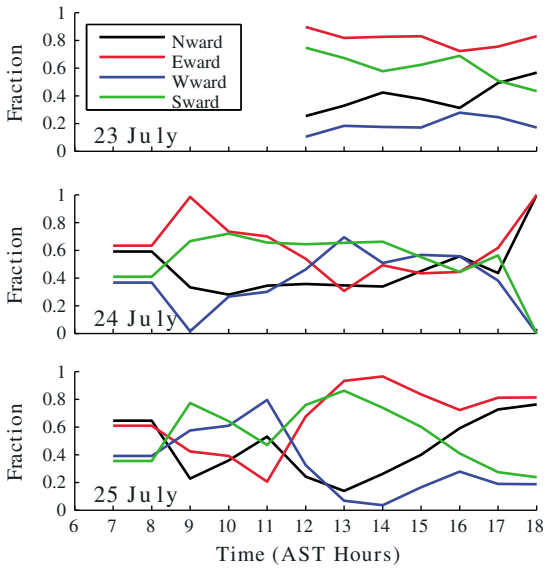

Figure 6. Fraction of waves propagating northward ($-90° < \phi < 90°$), southward ($-180° < \phi < -90°$,$90° < \phi < 180°$), eastward ($0° < \phi < 180°$), and westward ($-180° < \phi < 0°$) as a function of time in 2 h bins for all 3 days of observation.

The data from the 3 days are combined together in Figure 7, where we show the two-dimensional fractional histogram (i.e., normalized by the total number of waves in each time and angle bin) as a function of time and propagation direction. Overall, the main trend is for south-southeastward propagation during the morning, increasingly southeastward propagation by midday, and the appearance of a bimodal distribution of both southward-southeastward and northward-northeastward going waves in the late afternoon (although statistical significance is an issue in the morning and afternoon hours, and there is significant day-to-day variability). In addition to this main trend, waves are observed to propagate in most directions, except purely westward. Some southwestward and northwestward going waves are observed in the morning. Wave activity peaks in the early

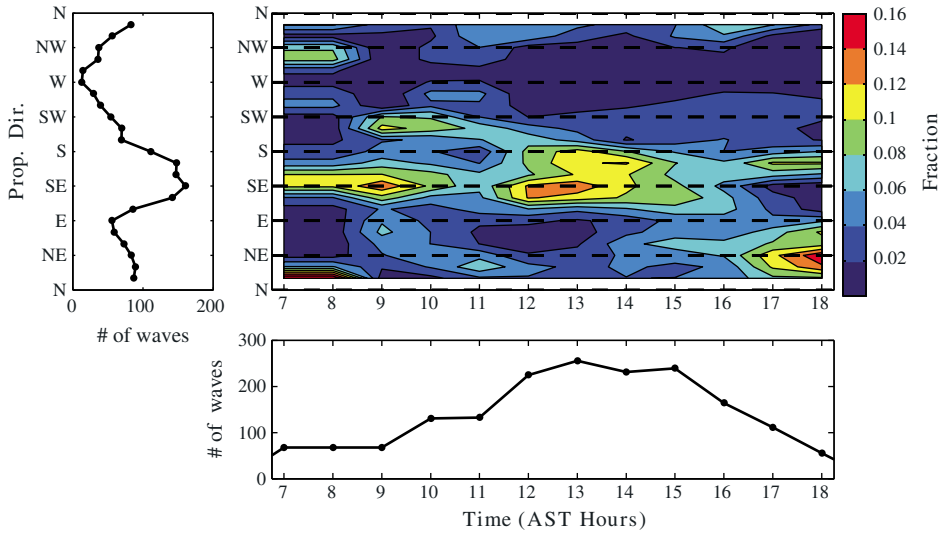

Figure 7. Binned and interpolated wave propagation histogram. The histogram has been normalized by the total number of waves within each time bin. Time bins are 2 h and are 50% overlapping. Angle bins are 30° and are also 50% overlapping. Line plots are one-dimensional histograms; i.e., summed over time (left) and angle (bottom), showing the total number of waves in each bin.

afternoon. The observation of southward propagating waves around midday, and the appearance of northward going waves in the late afternoon is not unlike the observations of *Jacobson et al.* [1995] and *Waldock and Jones* [1986], as discussed previously.

4.2. *E* Region Neutral Winds

The experiments undertaken at the AO allow us to determine the lower thermospheric/*E* region neutral winds by resolving the ion velocity vector and using the ion momentum equation [e.g., *Aponte et al.*, 2005; *Heinselman and Nicolls*, 2008; *Burchill et al.*, 2012] with a suitable model of the ion-neutral collision frequency, which we obtain using Mass Spectrometer Incoherent Scatter (MSIS) model [*Picone et al.*, 2002] parameters for a representative time near midday (12 AST = 16 UT) on 24 July 2009. This method allows us to determine the winds in regions where the ions are collisional, up to ~120–130 km altitude. Winds were computed using line-of-sight ion velocities averaged over an entire dwell period (40 or 60 min; see Table 1) and using temporally adjacent dwells to obtain the two components necessary to resolve the ion velocity vector. Thus, these winds represent averages over 80–120 min.

Wind profiles from 95 to 125 km for the 3 days are plotted in Figure 8. Cuts of wind magnitude and direction at specific altitudes (105–120 km) are plotted in Figure 9. The winds vary significantly with altitude and time. The winds tend to peak at 100-110 km with a magnitude of 100–200 m/s. These winds tend to be largest in the middle of the day at lower altitudes. These magnitudes and profiles are consistent with rocket-based chemical release determinations of wind vectors [e.g., *Larsen*, 2002]. The winds are strongest at low altitudes (100–110 km) and tend to rotate from north to east to south (i.e., clockwise) over the course of the day at ~105 km altitude. This rotation is consistent with the behavior of tides and large-scale, long-period waves in the Northern Hemisphere due to the action of the Coriolis force.

Any waves that reach the thermosphere from the lower atmosphere must propagate through winds of these magnitudes. In general, one would expect that waves propagating against the wind would be most favored to reach high altitudes in the thermosphere due to the combined effects of wind and dissipative filtering [e.g., *Waldock and Jones*, 1984; *Fritts and Vadas*, 2008]. However, Figure 8 shows that the winds rotate with altitude; thus, a given wave would likely experience large Doppler shifting at some altitude no matter what its propagation direction happened to be. In order to avoid reaching a critical level and dissipating, a wave must have a horizontal phase speed, c_H, that is greater than the wind component along the wave's propagation direction [*Fritts and Alexander*, 2003]. Given the rotation with altitude shown in Figure 8, then, we estimate that c_H must be greater than the maximum wind amplitude in the altitude range 100–110 km.

Figure 9 shows that the strongest winds tend to be northward near midday and shift to the south-southeastward direction by late afternoon at an altitude of ~105 km. This shifting of the winds may explain

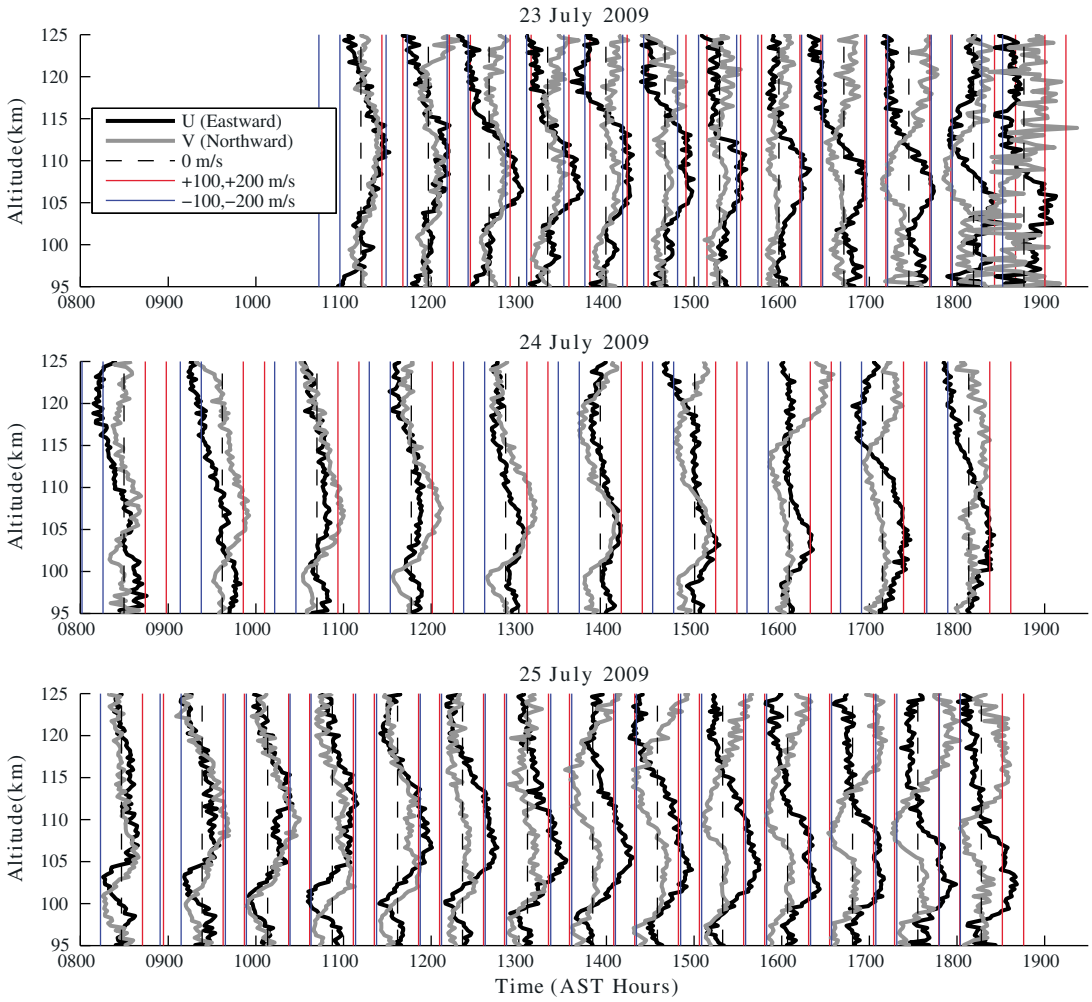

Figure 8. Resolved neutral winds in the *E* region and lower *F* region for the 3 days as function of time and altitude. Black lines (gray lines) correspond to zonal (meridional) winds. Vertical lines are at 0 m/s (dotted) 100 and 200 m/s (red solid line) and −100 and −200 m/s (blue solid line).

the appearance of stronger northward going wave activity in the late afternoon. However, if these winds are horizontally homogeneous over several hundred kilometers, then these winds cannot explain the absence of westward waves in Figures 5–7. For example, the peak in the winds at 105 km on 25 July is in the eastward direction at a magnitude of nearly 200 m/s, yet we observe strong eastward wave activity during this time and insignificant westward wave activity. Again, assuming spatial homogeneity of the winds, these strong lower thermospheric winds preclude the existence of low horizontal phase speed waves (in the example, the horizontal wave phase speeds must exceed 200 m/s). These parameters are examined in the next section.

4.3. Wave Dispersion

Figure 10 shows the amplitudes of all waves deemed statistically significant as a function of period (red dots). The binned results are shown as black bars and lines (see figure caption for details on these curves). As seen in Figures 2 and 3, the waves with the largest electron density amplitudes have periods greater than ~30 min and have amplitudes of 1% to 10%. Short-period waves (τ<20 min) typically have amplitudes less than 1%.

Figure 11 shows the horizontal wavelength (λ_H) and phase speed (c_H) as a function of propagation azimuth angle (ψ) and period (τ) for the 3 days of observations. Points are colored by the altitude of the measurements (see color bar) and median values and data distributions are also shown in a similar format to Figure 10. From Figure 11 (first and second rows), it is apparent that the low-altitude (z ~<150 km) waves are more isotropic in terms of propagation direction. They have smaller horizontal wavelengths and smaller

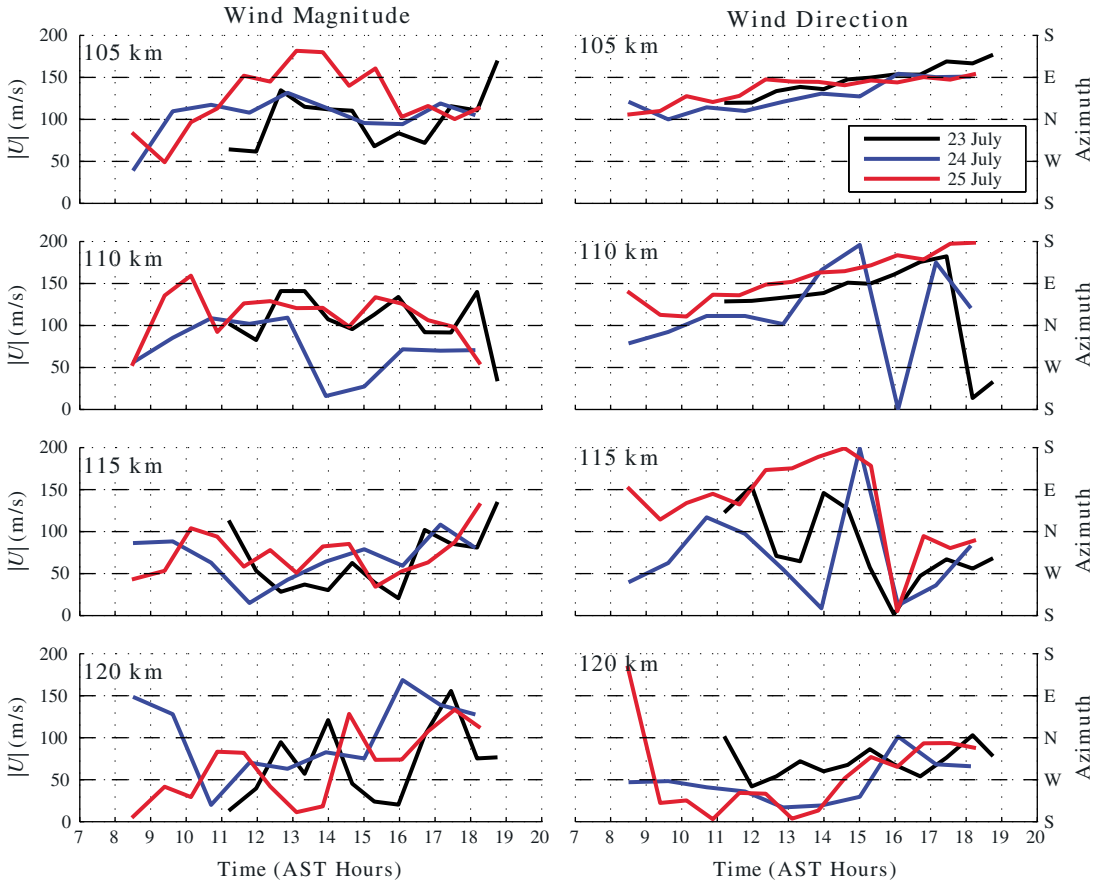

Figure 9. Wind magnitude and direction as a function of time at altitudes of 105 km, 110 km, 115 km, and 120 km for 23 (black), 24 (blue), and 25 (red) July.

phase speeds. From Figure 11 (third and fourth rows), we also see that these low-altitude waves have, in general, shorter periods. While the finding that these waves are roughly isotropic in propagation angle is apparent in the measurements and is quite interesting, we must be cautious about limitations of the measurement technique; as discussed earlier, an assumption in the analysis is of wavefield stationarity over multiple dwells. This may be violated for the smaller-scale, shorter-period waves. A future study will investigate these smaller-scale waves in more detail.

Figure 12 is the same as Figure 11 except colors represent time instead of altitude. Note that on 23 July, measurements did not begin until 1030 AST (see Table 1), so there are no early morning wave observations. Wind-filtering effects may be apparent by examination of the lowest phase speed waves observed. For example, on 25 July, two clusters of low ground-based phase speed waves are observed, one generally directed northward/northeastward generally late in the day, and the other directed southward/southeastward generally before noon. In the morning, the strong lower thermospheric winds were generally to the northeast and in the afternoon generally to the southeast (see Figure 9). Thus, these waves appear to be going against the strongest winds. However, it is important to emphasize that this observation is not clear all the time.

On 23 and 25 July, we see that the higher-altitude, larger-λ_H, larger-c_H waves are highly clustered in azimuth (Figure 11, first and second rows). These waves have c_H>200−300 m/s. Waves with c_H>300 m/s likely could not have propagated from (or been created) below $z\sim$ < 120 km (since the sound speed below 120 km is ~310 m/s). These waves could be secondary waves generated by GW dissipation or waves otherwise created in the lower thermosphere. In particular, a much smaller percentage of these waves propagate purely westward and northwestward. Because the diurnal tide is the main contributor to the background wind at z>200 km, if wind/dissipative filtering were the major mechanism for this anisotropy, the fraction

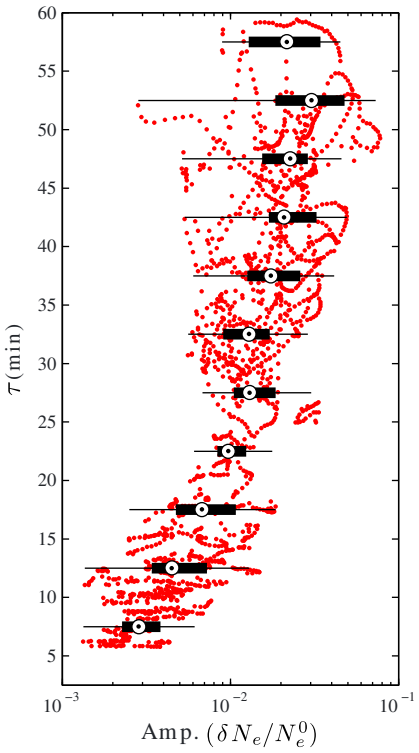

Figure 10. TID amplitude as a function of period for all days for every wave (red dots) and binned results (black bars and lines). In the distribution analysis, the central dot denotes the median of the data distribution, the black bar denotes the 25th to 75th percentile range, and the thin lines represent the full scatter of the data extending to the most extreme data points not considered outliers.

of westward waves would change significantly in time. However, as seen in Figure 12 (second row), there is no noticeable change in the percentage of high-c_H waves propagating westward over the 11 h observation window. Therefore, this result suggests that the sources of these waves are either anisotropically distributed around the AO or that wind filtering is occurring in another region of the atmosphere, such as by lower altitude stratospheric jets [e.g., *Brasseur and Solomon*, 2005] or mesospheric/lower thermospheric winds. Without knowledge of the background winds at these altitudes, our conclusions must be limited. In terms of wave phase speeds, all 3 days show similar trends. Horizontal wavelengths generally increase with increasing period, from ~100 km at small periods to ~400–500 km at large periods. Median wave phase speeds are in the range 100–300 m/s except for the largest-period waves, which have lower median phase speeds. There may be issues in determining the periods and/or horizontal wavelengths for these largest-period waves due to insufficient frequency resolution. The observation of wave phase speeds of the same order or larger than the lower thermospheric winds, especially for the waves observed in the lower thermosphere, implies that the *E* region neutral winds are efficient at removing low-speed waves. There is also an apparent increase in the phase speed for short-period waves. This effect is due to the increase of the GW vertical wavelength as the wave period approaches the buoyancy period (keeping λ_H fixed) [*Vadas*, 2007]; this increase allows the GW to propagate deeper into the thermosphere prior to dissipating. Using ray tracing, we will reproduce this effect theoretically below.

A summary of the wave parameters binned in altitude is shown in Figures 13a–13e, where again we plot waves deemed statistically significant (red dots) as well as bars representing the distribution of the data and median values. (We emphasize that these measurements are sensitive to a limited region of wave parameters, and thus, the median values should not be taken as representative of all waves.) Figure 13a shows the vertical wavelengths; we see an increase in the median value of $|\lambda_z|$ from ~< 50 km below ~150 km altitude to 100–300 km at z~200–300 km. The horizontal wavelengths (Figure 13b) also increase with altitude from ~100 km at the lowest altitudes to 150–500 km above 200 km altitude. As discussed earlier, the phase velocities (Figure 13c) tend to be greater than 100 m/s (the median values are ~200 m/s). This result is consistent with the lower thermospheric wind magnitudes for the waves observed in the lower thermosphere (i.e., the wind filters out the slower waves). It is also consistent with GW dissipative theory (i.e., for the GWs which dissipate above 125 km altitude, their intrinsic phase speeds are >100 m/s [*Vadas*, 2007]). A spread of ground-based wave periods is observed at all altitudes (Figure 13d), but in general higher-frequency waves are dominant at lower altitudes and lower frequency waves are dominant at higher altitudes. Finally, the amplitudes in Figure 13e show a maxima near 240 km, which is the bottomside of the *F* region. TID amplitudes diminish at higher altitudes because (1) the electron density perturbation amplitudes are proportional to the electron density gradient, which goes to zero at the *F* region peak [e.g., *Vadas and Nicolls*, 2009] and (2) the waves are dissipating.

Theoretical results were also obtained using the ray-tracing approach of *Vadas* [2007] (incorporating the dissipative GW dispersion relation of *Vadas and Fritts* [2005]). All GWs were ray traced through the NRLMSISE-00 background temperature profile on 24 July 2009 at 16 UT. White-noise (i.e., constant amplitude) GWs were ray traced through zero winds (Figures 13f–13m, red dots) and through a more realistic analytic tidal-like

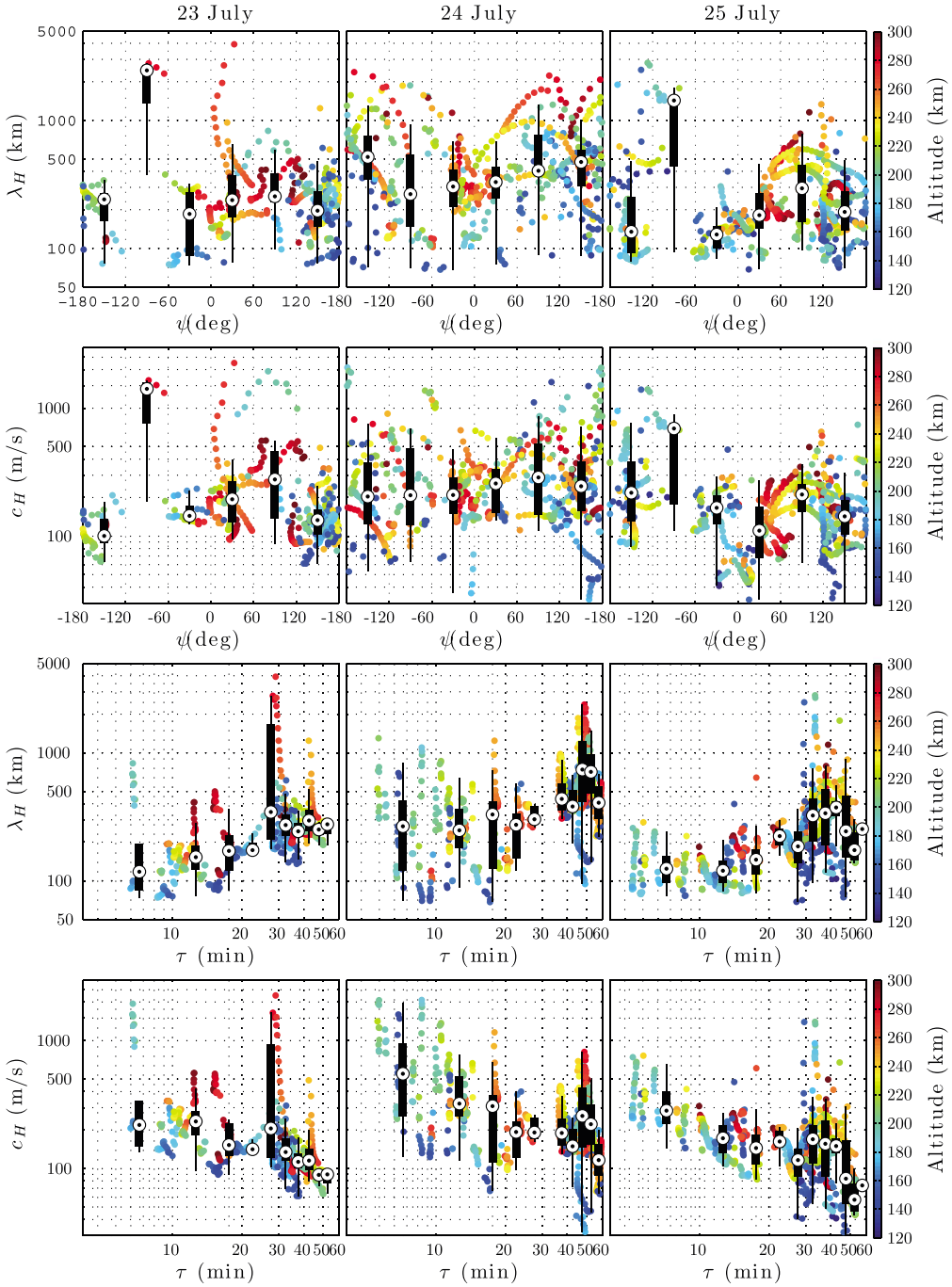

Figure 11. For each of the 3 days of observations (in columns): (first row) Horizontal wavelength (λ_H) as a function of propagation azimuth (ψ); (second row) Horizontal phase speed (c_H) as a function of propagation azimuth (ψ); (third row) Horizontal wavelength (λ_H) as a function of ground-based period (τ); (fourth row) Horizontal phase speed (c_H) as a function of ground-based period (τ). Points correspond to individual measurements and are colored by the altitude of the measurement (see color bar). Binned results (black bars and lines) represent a distribution analysis, with the central dot denoting the median of the data distribution, the black-filled bar denoting the 25th to 75th percentile range, and the thin lines represent the full scatter of the data extending to the most extreme data points not considered outliers.

wind profile that maximizes at z~60–90 km with an amplitude of 100 m/s, decreases exponentially above and below those altitudes, and rotates clockwise with altitude by 360° (Figures 13f–13m, black dots). White noise GWs (Figures 13f–13i) with horizontal wavelengths in the range 50 to 2000 km and vertical wavelengths in the range −10 to −500 km were launched at altitudes of 20, 150, and 180 km. Figures 13j–13m show the case of a restricted white-noise spectrum, which only allows GWs with periods <40 min to launch

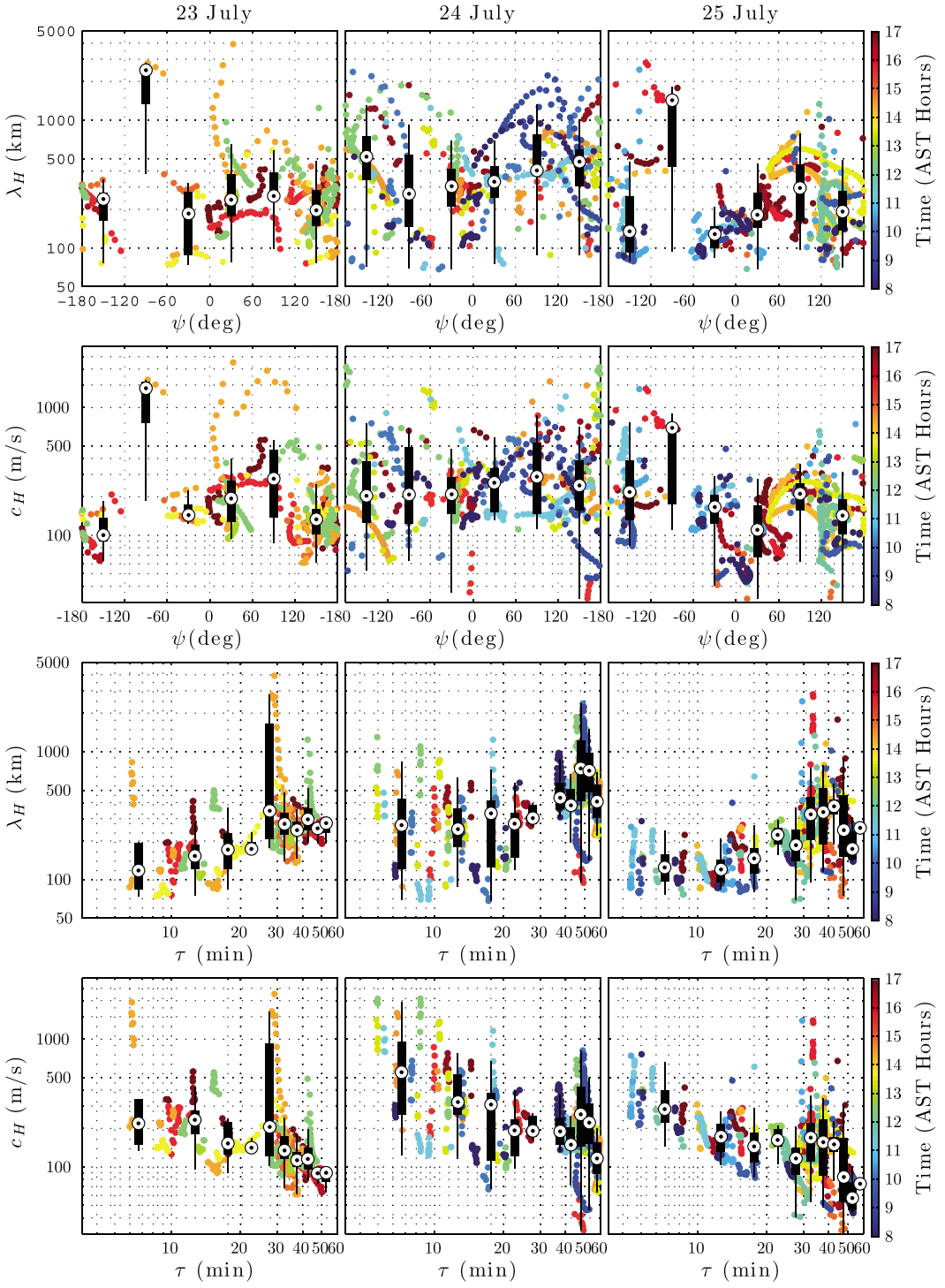

Figure 12. Same as Figure 11 except points are colored by Time in AST Hours (see color bar) instead of Altitude.

at z_i = 20 km, and which only allows GWs with periods >20 min and <60 min to launch at z_i = 150 and 180 km. These restrictions attempt to crudely mimic the expected wave scales from typical GW sources: convection and wave breaking in the lower atmosphere, and body force/heating in the thermosphere at z ~150–200 km [*Vadas and Crowley*, 2010; *Vadas*, 2013]. Note that each point is plotted at each GW's dissipation altitude, which is the altitude where the GW's momentum flux is maximum (defined as z_{diss}). A wave can and would be observed within ~1–2 density scale heights below and above z_{diss}.

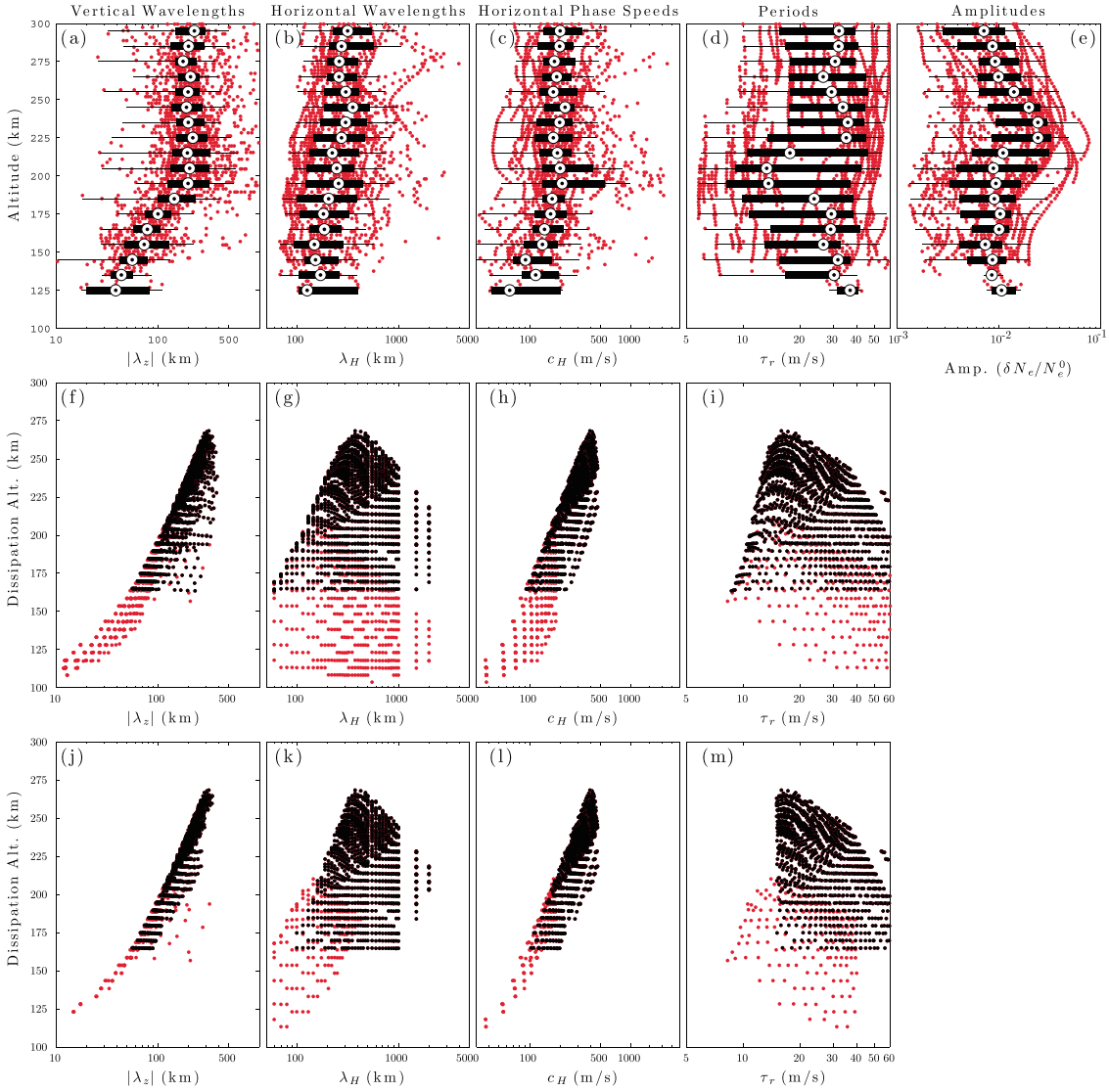

Figure 13. Scatterplot as a function of altitude for vertical wavelengths, horizontal wavelengths, horizontal phase speeds, periods, and TID amplitudes. (a–e) Individual waves (red points) and distribution analyses as in previous figures. Theoretical results are divided into two groups: (f–i) Results for white-noise gravity waves and (j–m) the same results but with a period limit (see text). Red points show a no-wind case, and black points show results using a more realistic wind profile (see text for details).

Notably, the white-noise case (Figure 13f) and the restricted case (Figure 13j) show vertical wavelength profiles very similar to the observations (Figure 13a) (also see *Vadas* [2007], Figure 9a). These curves show two distinct slopes: The vertical wavelength increases rapidly up to 150 km, then increases much more slowly above this altitude. This change in slope occurs because the kinematic viscosity increases more slowly with altitude as the thermospheric temperature increases. The horizontal wavelengths for the white-noise, no-wind case (Figure 13g, red points) show λ_H roughly uniform with altitude. However, as shown in Figure 13k, restricting the spectrum of waves leads to λ_H increasing with altitude, similar to the observations in Figure 13b. Waves ray traced through the analytic wind profile (Figure 13g, black points) have a similar, but less dramatic, effect. Finally, the variation of the horizontal wave phase speeds and ground-based periods is similar to the data (Figures 13h, 13i, 13l, and 13m), with somewhat better agreement for the restricted spectrum in the lower thermosphere. Overall, there is consistency between GW dissipative theory and the data, with caveats based on the assumptions in the ray tracing and background wind profiles (e.g., the thermospheric winds are assumed zero for the ray trace results shown in Figure 13, which is not realistic).

Theoretical curves of horizontal phase speed as a function of ground-based period (in this case equal to the intrinsic period, since the ray tracing assumes no thermospheric winds) for the white-noise, unrestricted

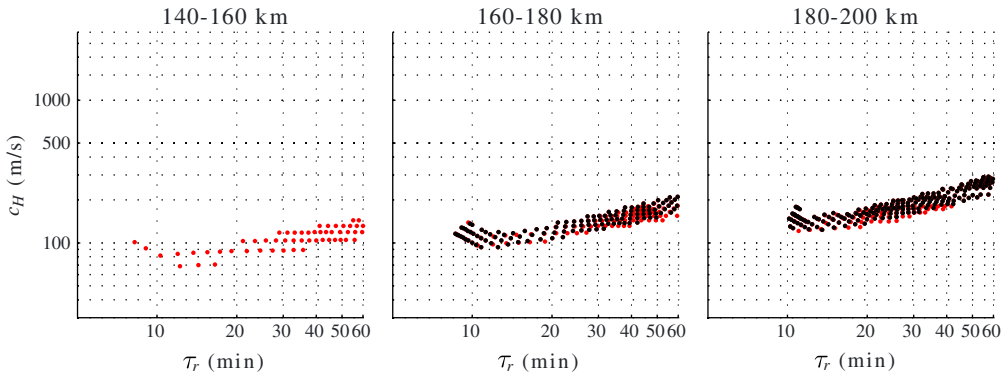

Figure 14. Horizontal phase speed as a function of ground-based period binned by dissipation altitude for white-noise gravity waves ray traced through no winds (red points) and a more realistic wind profile (black points; see text for details).

GWs are shown in Figure 14; here, the results have been binned in three altitude groups from 140 to 200 km. Similar to the measurements shown in Figures 11 and 12, the theoretical results show that wave phase speeds at all altitudes decrease with decreasing period until some period, at which point they begin to increase. For the white-noise GW case, this break point is at a period of about 12 min. A similar curve was shown in *Oliver et al.* [1997, Figure 8] with reference to the results of *Brownlie et al.* [1973] for the case where the exponential growth of a GW's amplitude is balanced by viscous dissipation. While providing qualitative agreement with the measurements, there are apparent differences. For example, the break points in Figures 11 and 12 tend to occur at somewhat larger periods of ~15–20 min. Additionally, the data curves are not uniform. These differences may be due to the effects of thermospheric winds and source specification effects, which will alter the dissipation curves, as well as potential limitations of the measurement technique.

We further examine the vertical wavelengths of those waves in Figure 15 which have the largest amplitudes (>0.3%) and which are observed consistently (>15 consecutive measurements in altitude). These waves are typically the longer-period, larger-amplitude waves that stand out in Figure 2. In this case, the vertical wavelengths are determined using running 1 h time series from the vertically looking beam, and thus, these waves are not necessarily associated with a horizontal wavelength measurement (since the GR data is not used in this analysis). We find the waves for a given 1 h period by taking cross spectra between adjacent range (altitude) gates and using a peak-finding algorithm to pick out statistically significant peaks. We then determine the periods and phase delays, as described previously. Waves are classified based on proximity in frequency and altitude. Spectral peaks that fall within 10 km altitude and within ~0.05 MHz are classified as the same wave. The wave period can thus vary with altitude; a typical total variation is ~10% of the median period. For waves traced greater than 100 km in altitude, the total variation is more typically in the range 15–20% or ~6–8 min in period. This variation of period with altitude is quite interesting and will be explored in future studies. We interpret these measurements as likely corresponding to waves at central/dominant frequencies in a GW packet. We also employ a correction for the vertical wavelength measurement as described in Appendix B. This correction accounts for the varying electron density scale height with altitude, which adds an additional phase offset to the electron density perturbation.

In Figure 15, we plot each vertically traced wave with the same color, with symbol sizes proportional to the TID (electron density) amplitude. The waves are divided into two separate bins based on the time of measurement for clarity purposes only. Figures 15a–15d and 15i–15l show their vertical wavelengths as a function of altitude. The median values (solid lines with error bars representing the standard deviation of the measurements) are also shown.

The median values show the increasing vertical-wavelength trend that was seen in Figure 13. In addition, plotted in gray is the evaluation of *Vadas* [2007, equation 15] (using MSIS values from 16 UT on 24 July), which shows the vertical wavelength at a given dissipation altitude for GWs with horizontal wavelengths of 500 km. By necessity, this curve covers a range of GW intrinsic periods [see *Vadas*, 2007, Figure 9]. This curve shows strong consistency with the measurements, as has been reported by *Djuth et al.* [2010].

The ion velocity perturbation created by a GW can be estimated from the corresponding electron density perturbation. Here, we assume that O^+ is the dominant ion, a good approximation above 200 km altitude,

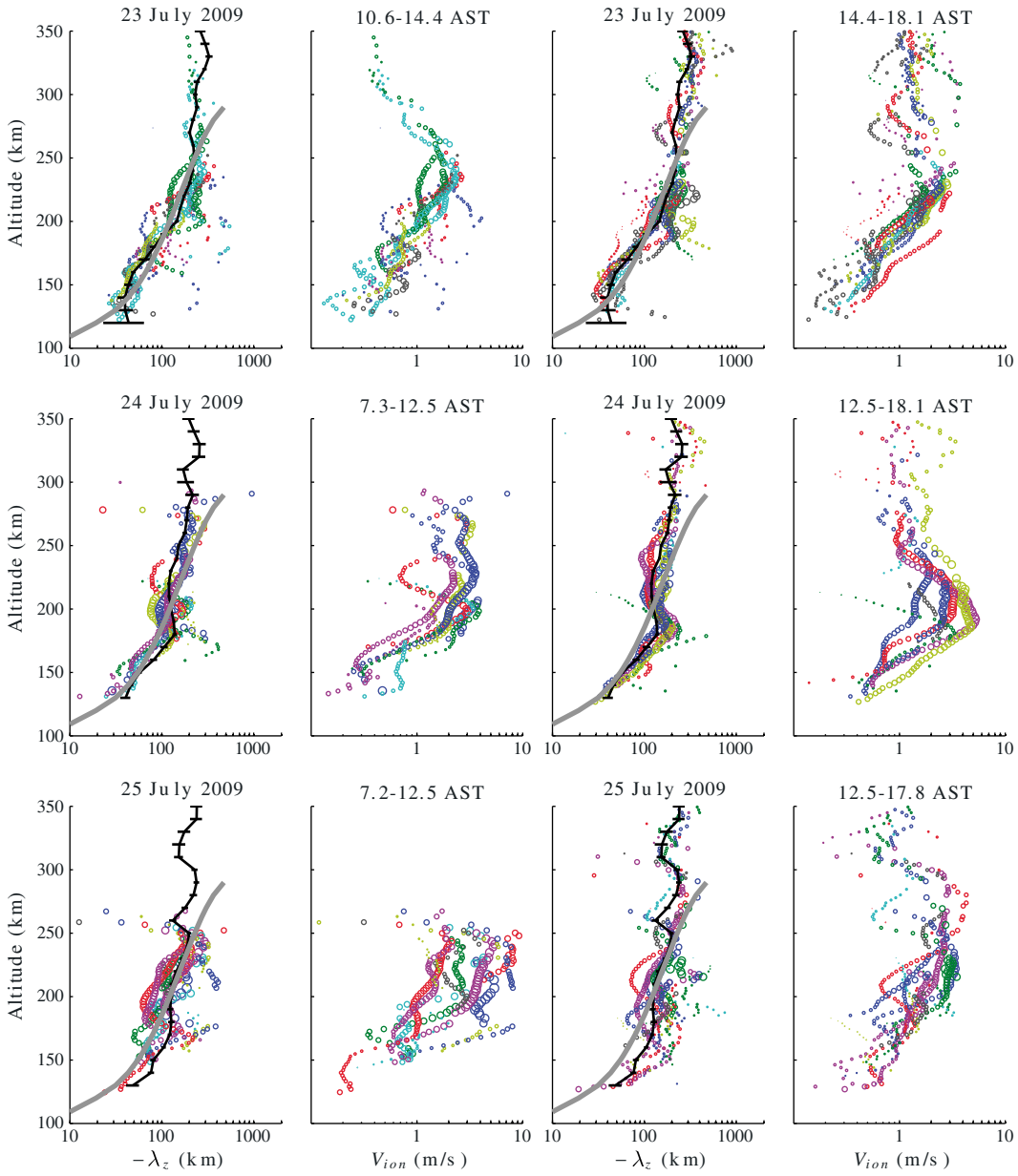

Figure 15. (columns 1 and 3) Vertical wavelengths (divided into two bins based on observation time) and (columns 2 and 4) calculated ion velocity perturbations as a function of altitude for each day (23 July on the top row, 24 July on the middle row, and 25 July on the bottom row). Waves are color coded and markers have a radius proportional to their TID amplitude. Here, waves have a minimum amplitude of 0.3% and are observed in at least 15 consecutive range gates. The black lines in columns 1 and 3 show the median values with standard errors. The gray line is the dissipation curve of *Vadas* [2007, equation 15] using MSIS model parameters from 16 UT on 24 July and a horizontal wavelength of 500 km.

and that the ions are magnetized so that the neutral winds of a GW perturb the ions along the geomagnetic field line. This calculation utilizes a linearized electron continuity equation. The relationship between the electron density (δN_{e0}) and ion velocity (v'_{i0}) perturbation amplitudes created by a GW (see derivation leading to equation (A17)) is

$$\frac{\delta N_{e0}}{\overline{N_e}} + i\frac{\overline{V}_z}{\omega_{\text{ion}}\overline{N_e}}\frac{\mathrm{d}(\delta N_{e0})}{\mathrm{d}z} = \frac{v'_{i0}}{\omega_{\text{ion}}}\left\{-i\frac{\sin I}{H_e} + (k_{H||}\cos I + m\sin I) - \frac{i\sin I}{v'_{i0}}\frac{\mathrm{d}v'_{i0}}{\mathrm{d}z}\right\}, \quad (4)$$

where ω_{ion} is the GW radian frequency Doppler shifted into the frame of the background ion drift (given by equation (A18)), I is the local magnetic dip angle ($I \sim 45°$ for Arecibo), $m = 2ß/\lambda_z$ is the vertical wavenumber,

$k_{H||} = k_H \cos(\psi - D)$ is the effective horizontal wavenumber of the GW projected onto the local magnetic field, ψ is the azimuthal angle of the propagation direction of the GW (positive east of north), D is the magnetic declination angle (~-22° at Arecibo), H_e is the electron density scale height, and $\overline{V}_z$ is the vertical component of the background ion drift velocity. (For further details and definitions, see Appendix A.) Here, we have neglected the production and loss of electrons due to chemical processes, drag, and friction. We have also assumed that the ion velocity approximately equals the component of the GW velocity parallel to the magnetic field. Setting $v'_{i0} \propto g(z)\exp(z/2H)$, where $\exp(z/2H)$ contains the increase from the decreasing neutral density and H is the neutral density scale height, and $g(z)$ contains the decrease from molecular viscosity, the amplitude of the ion velocity perturbation is (see equation (A20))

$$v'_{i0} \simeq \frac{\omega_{\text{ion}}}{\sin I}\left(\frac{\delta N_{e0}}{\overline{N}_e} + \frac{i\overline{V}_z}{\omega_{\text{ion}}\overline{N}_e}\frac{\mathrm{d}(\delta N_{e0})}{\mathrm{d}z}\right)\left\{k_{H||}\cot I + \left[m - i\left(\frac{1}{H_e} + \frac{1}{2H} + \frac{1}{g}\frac{\mathrm{d}g}{\mathrm{d}z}\right)\right]\right\}^{-1}. \quad (5)$$

Equation (5) states that the ion velocity perturbation depends on (i) the TID amplitude, (ii) the background density gradient, and (iii) both the vertical and horizontal wavelengths. Here we set $\mathrm{d}g/\mathrm{d}z = 0$. In doing so, we are only partly neglecting GW dissipation, because viscous dissipation is still taken into account via its effect on the (decreasing) amplitude of $\delta N_e/N_e^0$. Additionally, for simplicity, we ignore the background ion drift velocity here (i.e., set $\overline{V}_z = 0, \omega_{\text{ion}} \rightarrow \omega_r$). However, we note that it is straightforward to include these terms if the background drift velocity is known. Finally, the effective wavenumber $k_{H||}$ is almost always smaller than the true horizontal wavenumber k_H because the GW is infrequently oriented exactly along the magnetic field line. For GWs in the thermosphere, k_H is typically smaller than $|m|$; otherwise, the GW would likely become evanescent and reflect when it encountered small wind changes. If a GW's intrinsic period is much larger than the buoyancy period, then $k_H << |m|$ is automatically satisfied [*Fritts and Alexander*, 2003]. As can be seen from Figure 11, if the background neutral winds are small, this latter inequality is satisfied for most GWs above z>150 km, since the buoyancy period there is ~8–12 min. For these waves, $|k_{H||}| \ll |m|$. Therefore, we neglect the $k_{H||}$ (second) term in equation (5). In doing so, we note that it is not necessary to know a GW's horizontal wavelength in order to estimate its induced ion velocity perturbation from its electron density perturbation.

Using the above mentioned approximations, we estimate and plot the ion velocity perturbation amplitudes from equation (5) in Figure 15 (columns 2 and 4) for the waves shown in Figure 15 (columns 1 and 3, respectively), with the same color and marker size. We see from Figure 15 that individual waves often (but not always) show a peak in $|\lambda_z|$ at some altitude and decrease above that altitude. For the wave profiles shown here, this peak is often near 200 km altitude. The amplitude of the ion velocity perturbation tends to peak near or above this altitude, with a broad maximum often extending over a larger altitude range. Thus, while the overall, averaged values for the entire spectrum of waves show $|\lambda_z|$ increasing exponentially with altitude (see Figure 13a), individually traced waves generally show a maximum near the altitude where v'_{i0} is maximum, with a decrease in $|\lambda_z|$ to a constant (smaller) value above this altitude. Since v'_{i0} is approximately equal to the GW velocity perturbation along the direction of the magnetic field line, the altitude where v'_{i0} is maximum will likely be similar to the altitude where the GW's momentum flux is maximum (z_{diss}). Therefore, our results suggest that $|\lambda_z|$ generally maximizes near (or slightly below) z_{diss}. The finding that $|\lambda_z|$ maximizes near z_{diss} is consistent with the wave packet solution of the linearized Navier-Stokes equations [e.g., *Vadas*, 2007; *Vadas and Nicolls*, 2012] and of recent numerical results [*Liu et al.*, 2013]. Note that $|\lambda_z|$ may continue to slowly increase above z_{diss} if λ_H is relatively small [see *Vadas and Nicolls*, 2012, Figure 4a]; this is because z_{diss} occurs in the lower thermosphere in this case, where the background temperature is increasing. However, if λ_H is medium scale (~400–700 km), z_{diss} is higher, and $|\lambda_z|$ tends to maximizes at a somewhat lower altitude than z_{diss} (~10–30 km lower in the cases shown in *Vadas and Nicolls* [2012, Figures 4g and 4j]). Additionally, if the background wind varies substantially near z_{diss}, then $|\lambda_z|$ will behave differently than that predicted in a zero-wind environment.

Finally, we note that the TID amplitudes become maximum and then decrease with altitude for each wave packet (as represented by Figure 15, marker sizes). The maximum in the TID amplitude tends to occur at a lower altitude than the maximum in v'_{i0}, because the gradient of the background electron density is quite large at the bottomside of the F layer (see equation (4)).

5. Conclusion

We have reported on a comprehensive set of TID measurements on 23–25 July 2009 made at the Arecibo Observatory (AO) in Puerto Rico at low latitudes. The unique experiment allowed us to determine electron density perturbation amplitudes (or TID amplitudes), periods (up to 60 min), horizontal and vertical wavelengths, phase speeds, and propagation directions of daytime traveling ionospheric disturbances (TIDs) using dual-beam experiments with one beam looking vertically continuously and the other dwelling at two, 90° separated, azimuthal positions for 40–60 min.

As in previous studies, we find a near continuum of waves above the AO with TID activity peaking in the early afternoon local time. While the TIDs propagate in nearly all directions except purely westward, we find that most propagate southward-southeastward, especially on 23 and 25 July. However, the distribution is more isotropic on 24 July, with a clear shift from southeastward to northeastward in the late afternoon. In the aggregate, southward and southeastward TID propagation is observed to be dominant nearly all day except in the late afternoon, when northward going TIDs are observed.

We find that TID amplitudes increase nearly exponentially with increasing period, although with a much smaller slope for periods>30 min. The waves with the largest amplitudes have periods >30 min. TID amplitudes peak on the bottomside of the *F* region, as expected from the electron continuity equation. Typical vertical wavelengths increase from less than 50 km at low altitudes to ∼100–300 km in the mid-thermosphere. The aggregate vertical wavelengths plotted as a function of altitude show two distinctive slopes on a log scale, increasing rapidly up to ∼175 km and more slowly above that altitude. We ray traced individual white-noise GWs into the thermosphere using a dissipative GW model and found that the results agree well with the observations. In particular, the two distinctive slopes in the aggregate λ_z curve is due to the increasing thermospheric temperature, which causes the neutral density to decrease less rapidly in *z*, and the kinematic viscosity to increase less rapidly in *z* (as compared to in an isothermal atmosphere, such as approximately occurs in the lower atmosphere up to $z \sim 110$ km). Additionally, measured TID horizontal wavelengths were found to increase from ∼70–100 km in the lower thermosphere to ∼150–500 km in the mid-thermosphere. Via ray tracing, we found that the increase in λ_H in *z* might be due to wind filtering and/or the nature of the GW source spectrum.

On average, we found that the TID horizontal phase speeds are quite large, even in the lower thermosphere: >100–150 m/s. We also measured the lower thermospheric (*E* region) neutral, horizontal, mean winds. We found that they are quite strong, peaking at 150 m/s near $z \sim 105$ km in the middle of the day. These winds typically rotate with altitude and time, as expected if these winds are composed of tidal and other large-scale, long-period waves. We find that the TID horizontal phase speeds are in general greater than these ambient winds, in agreement with wind-filtering expectations. We note that some low-phase speed waves were observed for isolated time periods; these waves were found to be in general propagating against the strong lower thermospheric winds.

By tracing individual wave packets vertically in altitude, we find that each packet's vertical wavelength peaks near the altitude where its ion velocity amplitude is maximum. This result is consistent with gravity wave packet theory. In general, a wave packet's vertical wavelength tends to decrease with altitude above this altitude, until it reaches a constant (smaller) value.

Azimuth preferences may be caused by several factors, including wind filtering (by itself), dissipative and wind filtering combined, source location anisotropy, enhanced wave dissipation due to ion drag, and enhanced vertical ion motion driven preferentially by certain azimuth populations. The observation of high-altitude, high-phase speed wave activity with long-lasting preferential propagation directions suggests that location anisotropy may be a factor (although wind/dissipative filtering, for example from stratospheric jets, is expected to contribute). Given that the dominant propagation direction is southward and southeastward, these observations may imply dominant source regions in the southeastern U.S. However, conclusions concerning source regions are only speculative at this point and require detailed investigation of the wind environment throughout the atmosphere. In addition, observations in other seasons, where the wind and source environment is likely to be different, would also provide additional information.

With this short, 3 day data set, the generality of our conclusions are limited. However, because these observations and analyses result in the complete determination of gravity wave parameters, these and similar

data can be used in future studies to shed light on the sources of gravity waves reaching the ionosphere and thermosphere.

Appendix A: TIDs Induced by Gravity Waves—Single Ion Approximation

In this appendix, we derive simple linear expressions for the ion velocity and electron density perturbations induced by a GW. These expressions are similar to those derived in *Vadas and Nicolls* [2009], with slightly different notation, and with minor errors corrected. We assume that we are in a region of the ionosphere where only a single ion, O^+, dominates. We also neglect the production and loss of electrons due to chemical processes and some secondary dynamical effects.

Consider a GW propagating in the ψ direction, where ψ is the azimuth angle (clockwise from north), with wavenumber vector $\mathbf{k} = (k, \ell, m)$. The zonal and meridional components of this vector are

$$k = k_H \sin\psi, \quad \ell = k_H \cos\psi, \tag{A1}$$

where $k_H = \sqrt{k^2 + \ell^2}$. The GW's velocity vector can be written as follows:

$$\mathbf{u}' = (u'_0\,\hat{i} + v'_0\,\hat{j} + w'_0\,\hat{k})\exp(i\phi) \tag{A2}$$

where u'_0, v'_0, and w'_0 are the zonal, meridional, and vertical GW wind amplitudes, respectively; $\hat{i}$, $\hat{j}$, and $\hat{k}$ are the unit vectors in the geographic zonal, meridional, and vertical directions, respectively; and ϕ is the GW's phase given by

$$\phi = kx + \ell y + mz - \omega_r t. \tag{A3}$$

As the GW propagates, the neutral fluid particles that make up the GW collide with the ions in their path, imparting momentum to them. In the upper thermosphere, the ions are magnetized and only the neutral fluid momentum parallel to the magnetic field is transferred to the ions. Thus, in this region, the induced ion velocity perturbation is approximately equal to the projection of the GW's velocity vector along the magnetic field. We write the unit vector along the magnetic field as

$$\hat{\mathbf{B}} = \cos I \sin D\hat{i} + \cos I \cos D\hat{j} + \sin I\hat{k}. \tag{A4}$$

Here, I is the dip (inclination) angle, and D is the magnetic declination (or the angle, positive eastward, between magnetic and geographic north). The approximate ion velocity perturbation induced by the GW is then

$$\mathbf{v}'_i = v'_{i0}\exp(i\phi)\,\hat{\mathbf{B}}, \tag{A5}$$

where $v'_{i0}(z)$ is its amplitude, which may vary with altitude. Note that the phase of the ion velocity perturbation is expected to be the same as that of the GW. This amplitude can be calculated from equations (A2) and (A4):

$$v'_{i0} = (\mathbf{u}' \cdot \hat{\mathbf{B}}) \,/\, \exp(i\phi) = \cos I(u'_0 \sin D + v'_0 \cos D) + w'_0 \sin I. \tag{A6}$$

The GW phase, given by equation (A3), can be equivalently written with respect to coordinates (x_m, y_m) aligned along the local magnetic meridian; i.e., a clockwise rotation by the angle D:

$$x = x_m \cos D + y_m \sin D, \; y = y_m \cos D - x_m \sin D. \tag{A7}$$

(Note that this is a different coordinate system than that used by *Vadas and Nicolls* [2009].) Combining with equation (A1), we find that

$$\begin{aligned} kx + \ell y &= x_m k_H \sin(\psi - D) + y_m k_H \cos(\psi - D) \\ &= k_{H\perp} x_m + k_{H||} y_m, \end{aligned} \tag{A8}$$

where $k_{H||}$ and $k_{H\perp}$ are the components of the GW's horizontal wavenumber aligned with and perpendicular to the local magnetic meridian, respectively,

$$k_{H||} = k_H \cos(\psi - D), \quad k_{H\perp} = k_H \sin(\psi - D). \tag{A9}$$

(Equation (A8) corrects the equation stated between equations in *Vadas and Nicolls* [2009, equations 49 and 50].)

The electron density perturbation can be computed from the ion continuity equation ignoring production and loss,

$$\partial N_e/\partial t + \nabla \cdot (N_e \mathbf{v}_i) = 0, \tag{A10}$$

where N_e is the total electron density and $\mathbf{v}_i$ is the total ion velocity. We write the total ion velocity as a sum of the background ion drift velocity $\overline{\mathbf{V}}_i$ plus the perturbation induced by the GW:

$$\mathbf{v}_i = \overline{\mathbf{V}}_i + \mathbf{v}_i'. \tag{A11}$$

The background ion drift velocity is due to diffusion, winds, and other coupling processes. Similarly, we write the electron density as the sum of a background ($\overline{N_e}$) and perturbation (δN_e):

$$N_e = \overline{N_e} + \delta N_e. \tag{A12}$$

Plugging these expressions into equation (A10), the zeroth order expression (i.e., containing no perturbations) is

$$\nabla \cdot (\overline{N_e}\ \overline{\mathbf{V}}_i) = 0. \tag{A13}$$

Equation (A14) dictates the spatial arrangement of the background (unperturbed) ion drift velocity:

$$\nabla.\overline{\mathbf{V}}_i = -\frac{1}{\overline{N_e}}\overline{\mathbf{V}}_i.\nabla\overline{N_e}. \tag{A14}$$

If $\overline{N_e}$ only depends on z, we see that the divergence of the background ion velocity is only zero if the vertical component of the background ion velocity is zero. The first-order expression from equation (A10) is

$$\partial(\delta N_e)/\partial t + \nabla \cdot (\overline{N_e}\mathbf{v}_i') + \delta N_e \nabla \cdot \overline{\mathbf{V}}_i + \overline{\mathbf{V}}_i \cdot \nabla(\delta N_e) = 0. \tag{A15}$$

Inspection of equations (A15) and (A6) shows that the electron perturbation oscillates as $\exp(i\phi)$ with a possible additional phase shift. We write the electron density perturbation as

$$\delta N_e = \delta N_{e0}\ \exp(i\phi), \tag{A16}$$

where $\delta N_{e0}(z)$ is the complex amplitude, which varies as a function of altitude. Ignoring horizontal gradients in $\overline{N_e}$, equation (A15) becomes

$$\frac{\delta N_{e0}}{\overline{N_e}} + i\frac{\overline{V}_z}{\omega_{\text{ion}}\overline{N_e}}\frac{\mathrm{d}(\delta N_{e0})}{\mathrm{d}z} = \frac{v_{i0}'}{\omega_{\text{ion}}}\left\{-i\frac{\sin I}{H_e} + (k_{H||}\cos I + m\sin I) - \frac{i\sin I}{v_{i0}'}\frac{\mathrm{d}v_{i0}'}{\mathrm{d}z}\right\}, \tag{A17}$$

where we have defined the electron density scale height as $H_e = \overline{N_e}\left(\mathrm{d}\overline{N_e}/\mathrm{d}z\right)^{-1}$ and the Doppler shifted frequency as

$$\omega_{ion} = \omega_r - \overline{\mathbf{V}}_i \cdot \mathbf{k} - i\overline{V}_z/H_e. \tag{A18}$$

Here, $\overline{V}_z$ is the vertical component of $\overline{\mathbf{V}}_i$, and we have used $\nabla \cdot \overline{\mathbf{V}}_i = -\overline{V}_z/H_e$ from equation (A14). Note that equation (A17) is identical to *Vadas and Nicolls* [2009, equation 51] for zero background ion drift.

The last term in equation (A17) is proportional to the vertical gradient of the ion velocity amplitude. The amplitude of the ion velocity is proportional to the amplitude of the GW because the response is linear. The GW's amplitude increases as $\exp(z/2H)$ from the exponentially decreasing neutral density [*Hines*, 1960], where H is the neutral density scale height. At the same time, it decreases from viscous dissipation [*Vadas and Fritts*, 2005]. We parameterize this decrease by the function $g(z)$. Then, the ion velocity perturbation amplitude is proportional to $v_{i0}' \propto g(z)\exp(z/2H)$. Note that $g(z)$ is approximately constant at altitudes where viscosity is unimportant. At the dissipation altitude z_{diss} (where the GW's momentum flux is maximum), $g(z)\exp(z/2H)$ is approximately constant. At much higher altitudes, $g(z)\exp(z/2H)$ decreases with

altitude, although it is difficult to evaluate $g(z)$ analytically. Thus, $dv'_{i0}/dz \simeq v'_{i0}[1/2H + (1/g)dg/dz]$. With this approximation, equation (A17) becomes

$$\frac{\delta N_{e0}}{\overline{N_e}} + \frac{i\overline{V}_z}{\omega_{\text{ion}}\overline{N_e}}\frac{d(\delta N_{e0})}{dz} \simeq \frac{v'_{i0}}{\omega_{\text{ion}}}\left\{k_{H||}\cos I + \left[m - i\left(\frac{1}{H_e} + \frac{1}{2H} + \frac{1}{g}\frac{dg}{dz}\right)\right]\sin I\right\}. \tag{A19}$$

Note that the electron density perturbation amplitude $\delta N_{e0}/\overline{N_e}$ has both real and imaginary components. This implies that in general, there is a nontrivial phase shift between the ion velocity and electron density perturbations (see Appendix B).

If the electron density perturbation amplitude and the background ion velocity is known, the amplitude of the ion velocity perturbation can be calculated via

$$v'_{i0}(z) \simeq \frac{\omega_{\text{ion}}}{\sin I}\left(\frac{\delta N_{e0}}{\overline{N_e}} + \frac{i\overline{V}_z}{\omega_{\text{ion}}\overline{N_e}}\frac{d(\delta N_{e0})}{dz}\right)\left\{k_{H||}\cot I + \left[m - i\left(\frac{1}{H_e} + \frac{1}{2H} + \frac{1}{g}\frac{dg}{dz}\right)\right]\right\}^{-1}. \tag{A20}$$

The velocity vector of the ion perturbation is then given by equation (A5).

Appendix B: Phase Correction for λ_z Measurements

The vertical wavelength measurements described in this paper rely on a measurement of the electron density phase difference over an altitude range (δz). It is usual to equate the vertical wavenumber with the change in phase of the GW ($\delta\phi$) divided by δz. However, as we show in this appendix, there is an additional phase shift that is caused by the change in the electron density scale height as a function of altitude. Here, we derive a first-order correction to the phase in order to better estimate the vertical wavenumber of the GW.

We begin with equation (A19), and for this first-order correction neglect the background ion drift velocity as well as the dg/dz term (which has been discussed in section 4.3),

$$\frac{\delta N_{e0}}{\overline{N_e}} \simeq \frac{v'_{i0}}{\omega_{\text{ion}}}\left\{k_{H||}\cos I + \left[m - i\left(\frac{1}{H_e} + \frac{1}{2H}\right)\right]\sin I\right\}. \tag{B1}$$

We can then write the real and imaginary parts of this equation as

$$\begin{aligned}\text{Re}\left\{\frac{\delta N_{e0}}{\overline{N_e}}\right\} &= \frac{v'_{i0}}{\omega_r}\left(k_{H||}\cos I + m\sin I\right)\\ \text{Im}\left\{\frac{\delta N_{e0}}{\overline{N_e}}\right\} &= -\frac{v'_{i0}}{\omega_r}\left(\frac{1}{H_e} + \frac{1}{2H}\right)\sin I.\end{aligned} \tag{B2}$$

The phase of the perturbation amplitude is given by

$$\tan\xi = -\frac{1/H_e + 1/(2H)}{k_{H||}\cot I + m} \tag{B3}$$

The total phase, including the wave perturbation phase ϕ, is

$$\zeta = \xi + \phi. \tag{B4}$$

If we make phase measurement ζ_1 at some altitude z_1 and phase measurement ζ_2 at altitude $z_2 = z_1 + \delta z$ (at the same x, y, and t), then

$$\begin{aligned}\delta\zeta &= \zeta_2 - \zeta_1 = \xi_2 - \xi_1 + m\delta z\\ &= \tan^{-1}\left[\frac{1/H_{e1} + 1/(2H)}{k_{H||}\cot I + m}\right] - \tan^{-1}\left[\frac{1/H_{e2} + 1/(2H)}{k_{H||}\cot I + m}\right] + m\delta z\end{aligned} \tag{B5}$$

where we have let H_e vary, but assume all other terms are constant.

To simplify this expression, we use the series expansion $\tan^{-1}(x) \approx x + O(x^3)$. This first-order approximation is accurate to within 5–10%. Then,

$$\delta\zeta \approx \frac{1/H_{e1} - 1/H_{e2}}{k_{H||}\cot I + m} + m\delta z \approx \frac{\delta H_e}{H_{e1}^2}\left(\frac{1}{k_{H||}\cot I + m}\right) + m\delta z \tag{B6}$$

where we have defined $\delta H_e = H_{e2} - H_{e1}$ and expanded $1/(1 + \frac{\delta H_e}{H_{e1}})$ to first order. Note that in the limit that $\delta H_e = 0$, equation (B6) reduces to the expected expression

$$\delta\zeta = \delta\phi = m\delta z. \tag{B7}$$

Because $m < 0$ for an upward propagating GW, this implies that an upward propagating GW creates a negative phase change with altitude, $\delta\zeta < 0$ (for $\delta z > 0$), as is commonly known [*Fritts and Alexander*, 2003]. In the more general case that $\delta H_e \neq 0$, we can solve the quadratic equation for m:

$$m \approx \frac{1}{2\delta z}\left[(\delta\zeta - k_{H||}\cot I\delta z) + (\delta\zeta + k_{H||}\cot I\delta z)\sqrt{1 - 4\frac{\delta H_e}{H_{e1}^2}\frac{\delta z}{(\delta\zeta + k_{H||}\cot I\delta z)^2}}\right]. \tag{B8}$$

where we have chosen the solution that agrees with equation (B7) in the limit that $\delta H_e \to 0$. In the case that the correction is small, we can further expand the square root to obtain

$$m \approx \frac{\delta\zeta}{\delta z} - \frac{\delta H_e}{H_{e1}^2}\frac{1}{(\delta\zeta + k_{H||}\cot I\delta z)}. \tag{B9}$$

If we can further neglect the $k_{H||}$ term (see the discussion in section 4.3), then equation (B9) becomes

$$m \approx \frac{\delta\zeta}{\delta z} - \frac{\delta H_e}{H_{e1}^2}\frac{1}{\delta\zeta}. \tag{B10}$$

Acknowledgments

M.J.N. was supported by NSF grants AGS-1139152 and AGS-1242913. S.L.V. was supported by NSF grants AGS-1139149 and AGS-1242616. The Arecibo Observatory is operated by SRI International under a cooperative agreement with the National Science Foundation (AST-1100968) and in alliance with Sistema Universitario Ana G. Méndez and the Universities Space Research Association. The authors thank the reviewers for their constructive and detailed comments, which have improved the manuscript. M.J.N. thanks D. Drob for pointing out the importance of stratospheric jets.

Robert Lysak thanks Mike Kosch and an anonymous reviewer for their assistance in evaluating this paper.

References

Afraimovich, E. L., K. S. Palamartchouk, and N. P. Perevalova (1998), GPS radio interferometry of travelling ionospheric disturbances, *J. Atmos. Sol. Terr. Phys.*, *60*, 1205–1223.

Afraimovich, E. L., O. N. Boitman, E. I. Zhovty, A. D. Kalikhman, and T. G. Pirog (1999), Dynamics and anisotropy of traveling ionospheric disturbances as deduced from transionospheric sounding data, *Radio Sci.*, *34*, 477–488.

Afraimovich, E. L., E. A. Kosogorov, L. A. Leonovich, K. S. Palamartchouk, N. P. Perevalova, and O. M. Pirog (2000), Determining parameters of large-scale traveling ionospheric disturbances of auroral origin using GPS-arrays, *J. Atmos. Sol. Terr. Phys.*, *62*, 553–565.

Afraimovich, E. L., N. P. Perevalova, and S. V. Voyeikov (2003), Traveling wave packets of total electron content disturbances as deduced from global GPS network data, *J. Atmos. Sol. Terr. Phys.*, *65*, 1245–1262.

Aponte, N., M. J. Nicolls, S. A. González, M. P. Sulzer, M. C. Kelley, E. Robles, and C. A. Tepley (2005), Instantaneous electric field measurements and derived neutral winds at Arecibo, *Geophys. Res. Lett.*, *32*, L12107, doi:10.1029/2005GL022609.

Aponte, N., M. P. Sulzer, M. J. Nicolls, R. Nikoukar, and S. A. González (2007), Molecular ion composition measurements in the F1 region at Arecibo, *J. Geophys. Res.*, *112*, A06322, doi:10.1029/2006JA012028.

Behnke, R. (1979), *F* layer height bands in the nocturnal ionosphere over Arecibo, *J. Geophys. Res.*, *84*, 974–978.

Bowman, G. G. (1990), A review of some recent work on mid-latitude spread-F occurrence as detected by ionosondes, *J. Geomagn. Geoelec.*, *42*, 109–138.

Brasseur, G. P., and S. Solomon (2005), *Aeronomy of the Middle Atmosphere: Chemistry and Physics of the Stratosphere and Mesosphere*, Springer, Berlin.

Bristow, W., R. Greenwald, and J. Villain (1996), On the seasonal dependence of medium-scale atmospheric gravity waves in the upper atmosphere at high latitudes, *J. Geophys. Res.*, *101*(A7), 15,685–15,699.

Bristow, W. A., and R. A. Greenwald (1996), Multiradar observations of medium-scale acoustic gravity waves using the Super Dual Auroral Radar Network, *J. Geophys. Res.*, *101*, 24,499.

Bristow, W. A., R. A. Greenwald, and J. C. Samson (1994), Identifiaction of high-latitude acoustic gravity wave sources using the Goose Bay HF radar, *J. Geophys. Res.*, *99*, 319–331.

Brownlie, G. D., L. G. Dryburgh, and J. D. Whitehead (1973), Measurement of the dispersion of waves in the ionosphere, *Nat. Phys. Sci.*, *244*, 123–124.

Burchill, J. K., J. H. Clemmons, D. J. Knudsen, M. Larsen, M. J. Nicolls, R. F. Pfaff, D. Rowland, and L. Sangalli (2012), High-latitude *E* region ionosphere-thermosphere coupling: A comparative study using in situ and incoherent scatter radar observations, *J. Geophys. Res.*, *117*, A02301, doi:10.1029/2011JA017175.

Candido, C. M. N., A. A. Pimenta, J. A. Bittencourt, and F. Becker-Guedes (2008), Statistical analysis of the occurrence of medium-scale traveling ionospheric disturbances over Brazilian low latitudes using OI 630.0 nm emission all-sky images, *Geophys. Res. Lett.*, *35*(1), L17105, doi:10.1029/2008GL035043.

Crowley, G., T. B. Jones, and J. R. Dudeney (1987), Comparison of short period TID morphologies in Antarctica during geomagnetically quiet and active intervals, *J. Atmos. Terr. Phys.*, *49*, 1155–1162.

Crowley, G., and F. S. Rodrigues (2012), Characteristics of traveling ionospheric disturbances observed by the TIDDBIT sounder, *Radio Sci.*, *47*, RS0L22, doi:10.1029/2011RS004959.

Djuth, F. T., M. P. Sulzer, and J. H. Elder (1994), Application of the coded long-pulse technique to plasma line studies of the ionosphere, *Geophys. Res. Lett.*, *21*, 2725–2728.
Djuth, F. T., M. P. Sulzer, J. H. Elder, and V. B. Wickwar (1997), High-resolution studies of atmosphere-ionosphere coupling at Arecibo Observatory, Puerto Rico, *Radio Sci.*, *32*, 2321–2344, doi:10.1029/97RS02797.
Djuth, F. T., M. P. Sulzer, S. A. Gonzáles, J. D. Mathews, J. H. Elder, and R. L. Walterscheid (2004), A continuum of gravity waves in the Arecibo thermosphere?, *Geophys. Res. Lett.*, *31*, L16801, doi:10.1029/2003GL019376.
Djuth, F. T., L. D. Zhang, D. J. Livneh, I. Seker, S. M. Smith, M. P. Sulzer, J. D. Mathews, and R. L. Walterscheid (2010), Arecibo's thermospheric gravity waves and the case for an ocean source, *J. Geophys. Res.*, *115*, A08305, doi:10.1029/2009JA014799.
Dougherty, J. P., and D. T. Farley (1960), A theory of incoherent scattering of radio waves by a plasma, *Proc. R. Soc. London, Ser. A*, *259*, 79–99.
Fritts, D. C., and M. J. Alexander (2003), Gravity wave dynamics and effects in the middle atmosphere, *Rev. Geophys.*, *41*, 1003, doi:10.1029/2001RG000106.
Fritts, D. C., and S. L. Vadas (2008), Gravity wave penetration into the thermosphere: Sensitivity to solar cycle variations and mean winds, *Ann. Geophys.*, *26*, 3841–3861.
Garcia, F. J., M. C. Kelley, J. J. Makela, and C.-S. Huang (2000), Airglow observations of mesoscale low-velocity traveling ionospheric disturbances at midlatitudes, *J. Geophys. Res.*, *105*, 18,407–18,416.
Hernández-Pajares, M., J. M. Juan, and J. Sanz (2006), Medium-scale traveling ionospheric disturbances affecting GPS measurements: Spatial and temporal analysis, *J. Geophys. Res.*, *111*, A07S11, doi:10.1029/2005JA011474.
Heinselman, C. J., and M. J. Nicolls (2008), A Bayesian approach to electric field and *E*-region neutral wind estimation with the Poker Flat Advanced Modular Incoherent Scatter Radar, *Radio Sci.*, *43*, RS5013, doi:10.1029/2007RS003805.
Hines, C. O. (1960), Internal atmospheric gravity waves at ionospheric heights, *Can. J. Phys.*, *38*, 1441.
Hocke, K., and K. Schlegel (1996), A review of atmospheric gravity waves and travelling ionospheric disturbances: 1982–1995, *Ann. Geophys.*, *14*, 917–940.
Hocke, K., K. Schlegel, and G. Kirchengast (1996), Phases and amplitudes of TIDs in the high latitude F-region observed by EISCAT, *J. Atmos. Terr. Phys.*, *58*, 245–255.
Hooke, W. H. (1968), Ionospheric irregularities produced by internal atmospheric gravity waves, *J. Atmos. Terr. Phys.*, *30*, 795–823.
Hunsucker, R. D. (1982), Atmospheric gravity waves generated in the high-latitude ionosphere: A review, *Rev. Geophys. Space Phys.*, *20*, 293–315.
Isham, B., C. A. Tepley, M. P. Sulzer, Q. H. Zhou, M. C. Kelley, J. S. Friedman, and S. A. González (2000), Upper atmospheric observations at the Arecibo Observatory: Examples obtained using new capabilities, *J. Geophys. Res.*, *105*, 18,609–18,638.
Ishida, T., K. Hosokawa, T. Shibata, S. Suzuki, N. Nishitani, and T. Ogawa (2008), SuperDARN observations of daytime MSTIDs in the auroral and mid-latitudes: Possibility of long-distance propagation, *Geophys. Res. Lett.*, *35*, L13102, doi:10.1029/2008GL034623.
Jacobson, A. R., R. C. Carlos, R. S. Massey, and G. Wu (1995), Observations of traveling ionospheric disturbances with a satellite-beacon radio interferometer: Seasonal and local time behavior, *J. Geophys. Res.*, *100*, 1653–1665.
Kalikhman, A. D. (1980), Medium-scale travelling ionospheric disturbances and thermospheric winds in the *F*-region, *J. Atmos. Terr. Phys.*, *42*, 697–703.
Kelley, M. C. (2011), On the origin of mesoscale TIDs at midlatitudes, *Ann. Geophys.*, *29*, 361–366.
Kelley, M. C., and C. A. Miller (1997), Electrodynamics of midlatitude spread F 3. Electrohydrodynamic waves? A new look at the role of electric fields in thermospheric wave dynamics, *J. Geophys. Res.*, *102*, 11,539–11,548.
Kelley, M. C., and J. J. Makela (2001), Resolution of the discrepancy between experiment and theory of midlatitude *F*-region structures, *Geophys. Res. Lett.*, *28*(1), 2589–2592, doi:10.1029/2000GL012777.
Kirchengast, G., K. Hocke, and K. Schlegel (1996), The gravity wave-TID relationship: Insight via theoretical model—EISCAT data comparison, *J. Atmos. Terr. Phys.*, *58*, 233–243.
Klostermeyer, J. (1972), Numerical calculation of gravity wave propagation in a realistic thermosphere, *J. Atmos. Terr. Phys.*, *34*, 765–774.
Kotake, N., Y. Otsuka, T. Tsugawa, T. Ogawa, and A. Saito (2006), Climatological study of GPS total electron content variations caused by medium-scale traveling ionospheric disturbances, *J. Geophys. Res.*, *111*, A04306, doi:10.1029/2005JA011418.
Kotake, N., Y. Otsuka, T. Ogawa, T. Tsugawa, and A. Saito (2007), Statistical study of medium-scale traveling ionospheric disturbances observed with the GPS networks in Southern California, *Earth, Plan. Space*, *59*, 95–102.
Larsen, M. F. (2002), Winds and shears in the mesosphere and lower thermosphere: Results from four decades of chemical release wind measurements, *J. Geophys. Res.*, *107*(A8), SIA 28-1–SIA 28-14, doi:10.1029/2001JA000218.
Liu, C. H., and K. C. Yeh (1969), Effect of ion drag on propagation of acoustic-gravity waves in the atmospheric *F* region, *J. Geophys. Res.*, *74*, 2248–2255, doi:10.1029/JA074i009p02248.
Liu, X., J. Xu, J. Yue, and S. L. Vadas (2013), Numerical modeling study of the momentum deposition of small amplitude gravity waves in the thermosphere, *Ann. Geophys.*, *31*, 1–14.
Livneh, D. J., I. Seker, F. T. Djuth, and J. D. Mathews (2007), Continuous quasiperiodic thermospheric waves over Arecibo, *J. Geophys. Res.*, *112*, A07313, doi:10.1029/2006JA012225.
Martinis, C., J. Baumgardner, J. Wroten, and M. Mendillo (2010), Seasonal dependence of MSTIDs obtained from 630.0 nm airglow imaging at Arecibo, *Geophys. Res. Lett.*, *37*, L11103, doi:10.1029/2010GL043569.
Mendillo, M., J. Baumgardner, D. Nottingham, J. Aarons, B. Reinisch, J. Scali, and M. Kelley (1997), Investigations of thermospheric-ionospheric dynamics with 6300-Å images from the Arecibo Observatory, *J. Geophys. Res.*, *102*, 7331–7344.
Miller, C. A. (1997), Electrodynamics of midlatitude spread F 2. A new theory of gravity wave electric fields, *J. Geophys. Res.*, *102*, 11,533–11,538.
Morton, F. W., and E. A. Essex (1978), Gravity wave observations at a Southern Hemisphere mid-latitude station using the total electron content technique, *J. Atmos. Terr. Phys.*, *40*, 1113–1122.
Nicolls, M. J., and C. J. Heinselman (2007), Three-dimensional measurements of traveling ionospheric disturbances with the Poker Flat Incoherent Scatter Radar, *Geophys. Res. Lett.*, *34*, L21104, doi:10.1029/2007GL031506.
Nicolls, M. J., M. C. Kelley, A. J. Coster, S. A. González, and J. J. Makela (2004), Imaging the structure of a large-scale TID using ISR and TEC data, *Geophys. Res. Lett.*, *31*, L09812, doi:10.1029/2004GL019797.
Nicolls, M. J., M. P. Sulzer, N. Aponte, R. Seal, R. Nikoukar, and S. A. González (2006), High-resolution electron temperature measurements using the plasma line asymmetry, *Geophys. Res. Lett.*, *33*, L18107, doi:10.1029/2006GL027222.
Nicolls, M. J., R. H. Varney, S. L. Vadas, P. A. Stamus, C. J. Heinselman, R. B. Cosgrove, and M. C. Kelley (2010), Influence of an inertia-gravity wave on mesospheric dynamics: A case study with the Poker Flat Incoherent Scatter Radar, *J. Geophys. Res.*, *115*, D00N02, doi:10.1029/2010JD014042.

Ogawa, T., N. Nishitani, Y. Otsuka, K. Shiokawa, T. Tsugawa, and K. Hosokawa (2009), Medium-scale traveling ionospheric disturbances observed with the SuperDARN Hokkaido radar, all-sky imager, and GPS network and their relation to concurrent sporadic E irregularities, *J. Geophys. Res.*, *114*, A03316, doi:10.1029/2008JA013893.

Oliver, W. L., S. Fukao, Y. Yamamoto, T. Takami, M. D. Yamanaka, M. Yamamoto, T. Nakamura, and T. Tsuda (1994), Middle and upper atmosphere radar observations of ionospheric density gradients produced by gravity wave packets, *J. Geophys. Res.*, *99*, 6321–6329, doi:10.1029/94JA00171.

Oliver, W. L., S. Fukao, M. Sato, Y. Otsuka, T. Takami, and T. Tsuda (1995), Middle and upper atmosphere radar observations of the dispersion relation for ionospheric gravity waves, *J. Geophys. Res.*, *100*, 23,763–23,768, doi:10.1029/95JA02520.

Oliver, W. L., Y. Otsuka, M. Sato, T. Takami, and S. Fukao (1997), A climatology of *F* region gravity wave propagation over the middle and upper atmosphere radar, *J. Geophys. Res.*, *102*, 14,499–14,512.

Otsuka, Y., K. Shiokawa, T. Ogawa, and P. Wilkinson (2004), Geomagnetic conjugate observations of medium-scale traveling ionospheric disturbances at midlatitude using all-sky airglow imagers, *Geophys. Res. Lett.*, *31*, L15803, doi:10.1029/2004GL020262.

Picone, J. M., D. P. Drob, and A. C. Aikin (2002), Nrlmsise-00 empirical model of the atmosphere: Statistical comparisons and scientific issues, *J. Geophys. Res.*, *107*(A12), 1468, doi:10.1029/2002JA009430.

Saito, A., S. Fukao, and S. Miyazaki (1998), High resolution mapping of TEC perturbations with the GSI GPS network over Japan, *Geophys. Res. Lett.*, *25*, 3079–3082.

Saito, A., et al. (2001), Traveling ionospheric disturbances detected in the FRONT campaign, *Geophys. Res. Lett.*, *28*, 689–692, doi:10.1029/2000GL011884.

Salpeter, E. E. (1960), Electron density fluctuations in a plasma, *Phys. Rev.*, *120*, 1528–1535.

Salpeter, E. E. (1961), Plasma density fluctuations in a magnetic field, *Phys. Rev.*, *122*, 1663–1674.

Seker, I., D. J. Livneh, and J. D. Mathews (2009), A 3-D empirical model of *F* region medium-scale traveling ionospheric disturbance bands using incoherent scatter radar and all-sky imaging at Arecibo, *J. Geophys. Res.*, *114*, A06302, doi:10.1029/2008JA014019.

Seker, I., S. F. Fung, and J. D. Mathews (2011), Relation between magnetospheric state parameters and the occurrence of plasma depletion events in the nighttime midlatitude *F* region, *J. Geophys. Res.*, *116*, A04323, doi:10.1029/2010JA015521.

Shiokawa, K., Y. Otsuka, C. Ihara, T. Ogawa, and F. J. Rich (2003a), Ground and satellite observations of nighttime medium-scale traveling ionospheric disturbance at midlatitude, *J. Geophys. Res.*, *108*, 1052, doi:10.1029/2002JA009491.

Shiokawa, K., C. Ihara, Y. Otsuka, and T. Ogawa (2003b), Statistical study of nighttime medium-scale traveling ionospheric disturbances using midlatitude airglow images, *J. Geophys. Res.*, *108*, 1145, doi:10.1029/2002JA009639.

Shiokawa, K., Y. Otsuka, and T. Ogawa (2006), Quasiperiodic southward moving waves in 630-nm airglow images in the equatorial thermosphere, *J. Geophys. Res.*, *111*, A06301, doi:10.1029/2005JA011406.

Sulzer, M. P. (1986a), A radar technique for high range resolution incoherent scatter autocorrelation function measurements utilizing the full average power of klystron radars, *Radio Sci.*, *21*(6), 1033–1040.

Sulzer, M. P. (1986b), A phase modulation technique for a sevenfold statistical improvement in incoherent scatter data-taking, *Radio Sci.*, *21*, 737–744.

Tsugawa, T., Y. Otsuka, A. J. Coster, and A. Saito (2007), Medium-scale traveling ionospheric disturbances detected with dense and wide TEC maps over North America, *Geophys. Res. Lett.*, *34*, L22101, doi:10.1029/2007GL031663.

Vadas, S. L. (2007), Horizontal and vertical propagation and dissipation of gravity waves in the thermosphere from lower atmospheric and thermospheric sources, *J. Geophys. Res.*, *112*, A06305, doi:10.1029/2006JA011845.

Vadas, S. L. (2013), Compressible *F*-plane solutions to body forces, heatings, and coolings; and application to the primary and secondary-thermospheric gravity waves generated by a deep convective plume, *J. Geophys. Res. A: Space Phys*, *118*, 2377–2397, doi:10.1002/jgra.50163.

Vadas, S. L., and G. Crowley (2010), Sources of the traveling ionospheric disturbances observed by the ionospheric TIDDBIT sounder near Wallops Island on 30 October 2007, *J. Geophys. Res.*, *115*, A07324, doi:10.1029/2009JA015053.

Vadas, S. L., and D. C. Fritts (2005), Thermospheric responses to gravity waves: Influences of increasing viscosity and thermal diffusivity, *J. Geophys. Res.*, *110*, D15103, doi:10.1029/2004JD005574.

Vadas, S. L., and M. J. Nicolls (2008), Using PFISR measurements and gravity wave dissipative theory to determine the neutral, background thermospheric winds, *Geophys. Res. Lett.*, *35*, L02105, doi:10.1029/2007GL031522.

Vadas, S. L., and M. J. Nicolls (2009), Temporal evolution of neutral, thermospheric winds and plasma response using PFISR measurements of gravity waves, *J. Atmos. Solar-Terr. Phys.*, *71*, 744–770, doi:10.1016/j.jastp.2009.01.011.

Vadas, S. L., and M. J. Nicolls (2012), The phases and amplitudes of gravity waves propagating and dissipating in the thermosphere: Theory, *J. Geophys. Res.*, *117*, A05322, doi:10.1029/2011JA017426.

Waldock, J. A., and T. B. Jones (1984), The effects of neutral winds on the propagation of medium-scale atmospheric gravity waves at mid-latitudes, *J. Atmos. Terr. Phys.*, *46*, 217–231.

Waldock, J. A., and T. B. Jones (1986), HF Doppler observations of medium-scale travelling ionospheric disturbances at mid-latitudes, *J. Atmos. Terr. Phys.*, *48*, 245–260.

Waldock, J. A., and T. B. Jones (1987), Source regions of medium scale travelling ionospheric disturbances observed at mid-latitudes, *J. Atmos. Terr. Phys.*, *49*, 105–114.